Temporal Changes of Shear Wave Velocity and Anisotropy in the Shallow Crust Induced by the 10/22/1999 M6.4 Chia-Yi, Taiwan Earthquake

A Thesis
Presented to
The Academic Faculty

by

Tzu-Kai Kevin Chao

In Partial Fulfillment
of the Requirements for the Degree
Master of Science in the
School of Earth and Atmospheric Sciences

Georgia Institute of Technology
May 2009

Temporal Changes of Shear Wave Velocity and Anisotropy in the Shallow Crust Induced by the 10/22/1999 M6.4 Chia-Yi, Taiwan Earthquake

Approved by:

Dr. Zhigang Peng, Advisor
School of Earth and Atmospheric Sciences
Georgia Institute of Technology

Dr. Andrew V. Newman
School of Earth and Atmospheric Sciences
Georgia Institute of Technology

Dr. Dominic Assimaki
School of Civic and Environmental Engineering
Georgia Institute of Technology

Date Approved: April 4, 2009

ACKNOWLEDGEMENTS

The person I would like to thank most is my advisor Dr. Zhigang Peng. Without his patience and inspiration throughout my study, I wouldn't have learnt so much, not only on the professional knowlege, but also the spirit of dedication toward research. I would also like to thank Dr. Andrew V. Newman and Dr. Dominic Assimaki for spending time as my committee members. And of course I'm grateful to all my other colleagues in Geophysical group and EAS for their support and encouragement.

Last but not least, I want to thank my parents and my dear wife Erica for their support and faith in me. To my new born son Adam, you are the best reward.

TABLE OF CONTENTS

LIST OF FIGURES

SUMMARY

Temporal changes of seismic velocity and anisotropy in the shallow crust are quantified using local earthquakes recorded at a 200-m-deep borehole station CHY in Taiwan. This station is located directly above the hypocenter of the 10/22/1999, M6.4 Chia-Yi earthquake. Three-component seismograms recorded at this station show clear direct (up-going) and surface-reflected (down-going) *P*- and *S*-waves, and *S*-wave splitting signals. The two-way travel times in the top 200 m is obtained by measuring the time delays between the up-going and down-going waves in the auto-correlation function. The *S*-wave travel times measured in two horizontal components increase by ~1-2% at the time of Chia-Yi main shock, and followed by a logarithmic recovery, while the temporal changes of *S*-wave splitting and *P*-wave are less than 1% and are not statistically significant. We obtain similar results by grouping earthquakes into clusters according to their locations and waveform similarities. This suggests that the observed temporal changes are not very sensitive to the seismic ray path below CHY, but are mostly controlled by the variation of material property in the top 200 m of the crust. We propose that strong ground motions of the Chia-Yi main shock cause transient openings of fluid-filled microcracks and increases the porosity in the near-surface layers, followed by a relatively long healing process. Because we observe no clear changes in the shear wave anisotropy, we infer that the co-seismic damages do not have a preferred orientation. Our results also show a gradual increase of time delays for both the fast and slow *S*-waves in the previous 7 years before the Chia-Yi main shock. Such changes might be caused by variations of water table, sediment packing or other surficial processes.

CHAPTER 1

INTRODUCTION

The top few hundred meters of the shallow crust is heavily fractured, and is characterized by extremely low shear wave velocity (~200-400 m/s) and very high attenuation (Q ~1-10) (e.g. Aster & Shearer 1991b). If the fractures are preferentially aligned, seismic shear waves propagating through such shallow anisotropic layer are expected to split into two orthogonally polarized waves with different velocities. This phenomenon is analogous to optical birefringence and is termed shear wave splitting (SWS). Two routinely determined splitting parameters are the polarization direction of the fast wave (φ) and the delay time (δt) between the fast and slow waves. The obtained magnitude of shear wave anisotropy in the shallow crust is typically in the range of 5-20%, and decreases systematically with increasing depth (e.g. Daley & McEvilly 1990; Aster & Shearer 1991a; Coutant 1996; Liu *et al.* 2004, 2005a; Boness & Zoback 2004, 2006; Peng & Ben-Zion 2004). This is mainly because increasing normal stress at depth tends to close fractures and microcracks, resulting in reduced shear wave anisotropy. The elastic and anisotropic properties of the shallow crust can be further modulated by strong ground motions of nearby earthquakes, and other processes that operate under very low normal stress conditions. These include changes in the water table, weathering processes, seasonal thermoelastic strain, and solid earth tides.

Observing temporal changes of material properties in the upper crust has been a long-sought goal of the geophysics community for many decades. A better quantification of temporal changes in the near-surface layers is crucial for improved understandings of rock rheology in the shallow crust, better characterization of site responses, and accurate predictions of strong ground

motions for future large earthquakes. Numerous laboratory studies over the past few decades have found a clear stress dependence of elastic and anisotropic properties for crustal rocks and near-surface layers (e.g. Scholz 1968; Nur & Simmons 1969). Such stress dependence is mainly caused by the opening/closure of microcracks or changes of porosity due to changes in normal stresses (e.g. Nur 1971; Crampin & Zatsepin 1997). Because of this, it is possible to detect temporal changes of material properties and stress variations by monitoring time-varying seismic properties.

Using natural earthquake sources, many earlier studies have observed large temporal changes in the travel times of *P* and *S* arrivals, or scattering properties in the *S*-coda waves (e.g. Whitcomb *et al.* 1973; Jin & Aki 1986). However, these studies were not generally convincing, mainly due to uncertainties associated with earthquake locations and origin times (e.g. McEvilly & Johnson 1974; Kanamori & Fuis 1976; Beroza *et al.* 1995). Recent studies based on waveform cross-correlations of repeating earthquakes have found small but resolvable changes of seismic velocities in shallow surface layers and around active FZ associated with the occurrences of major earthquakes or aseismic slip events (e.g. Poupinet *et al.* 1984; Niu *et al.* 2003; Schaff & Beroza 2004; Rubinstein & Beroza 2004a, b, 2005; Peng & Ben-Zion 2006; Li *et al.* 2006; Rubinstein *et al.* 2007; Taira *et al.* 2008a, b; Zhao & Peng 2008; Toteva *et al.* 2008). The observed temporal changes in seismic velocities, typically on the order of a few percent or less, are characterized by rapid reductions during strong motions of nearby large earthquakes, followed by logarithmic recoveries on the time scales of several months to years. The use of repeating earthquakes allows the separation of temporal changes of material properties from spatial variations of earthquake locations (e.g. Liu *et al.* 2004, 2005a; Peng & Ben-Zion 2005, 2006). However, repeating earthquakes only occur in certain locations and their occurrence times

cannot be controlled. Some recent studies also employed repeating artificial sources (e.g. Li *et al.* 1998, 2006; Matsumoto *et al.* 2001; Vidale & Li 2003; Silver *et al.* 2007; Niu *et al.* 2008) and found similar results. But these types of studies are limited by high cost and poor depth penetration.

While temporal changes of seismic velocities in the shallow crust have been well documented, the results on temporal changes of SWS are still controversial. Using natural earthquakes, a number of studies have found temporal changes of splitting parameters before (e.g. Crampin *et al*. 1990, 1991, 1999; Gao *et al.* 1998; Crampin & Gao 2005), during (e.g. Saiga *et al.* 2003) and after (e.g. Tadokoro & Ando 2002; Hiramatsu *et al.* 2005) major events or earthquake swarms. However, other studies did not find any clear changes of crustal anisotropy near the epicentral regions of major earthquakes (e.g. Aster *et al.* 1990, 1991; Savage *et al.* 1990; Munson *et al*. 1995; Cochran *et al.* 2003, 2006; Liu *et al.* 2004). Systematic analysis based on repeating earthquakes also found no observable temporal changes in SWS associated with the 1999 Mw7.1 Duzce (Peng & Ben-Zion 2005), the 1999 Mw7.6 Chi-Chi (Liu *et al.* 2005a), and the 2004 Mw6.0 Parkfield earthquake (Liu *et al.* 2008). Using Accurately Controlled Routinely Operated Signal System (ACROSS), Ikuta & Yamaoka (2004) found ~0.4% changes in shear-wave anisotropy associated with nearby earthquakes. These results suggest that temporal changes in anisotropy caused by large earthquakes may be observable, although the amplitudes of the changes could be much smaller than those associated with direct measurements in seismic velocities.

In this study, we quantify temporal changes of seismic velocity and shear-wave anisotropy in the shallow crust using local earthquakes recorded at a 200-m-deep borehole station CHY in Taiwan (Figure 1). This station is located directly above the hypocenter of the

10/22/1999, M6.4 Chia-Yi earthquake, and has recorded many small earthquakes with clear surface reflected waves and shear wave splitting signals. Liu *et al.* (2004, 2005a, 2005b) have systematically analyzed temporal change of SWS and attenuation anisotropy at this station before and after the 09/20/1999 Mw7.6 Chi-Chi earthquake, and the M6.4 Chia-Yi earthquake occurred about one month later. They concluded that the SWS delay times do not show significant changes associated with the Chi-Chi and the Chia-Yi earthquakes. This study is motivated by the results of Liu *et al.* (2004, 2005a), but differs from their work in the following aspect. First, Liu *et al.* (2004, 2005a) only measured the temporal changes in SWS delay time δt at station CHY. Here, we apply a similar technique to measure the time delay (TD) between clear incident (up-going) and surface-reflected (down-going) signals, and quantify temporal changes in the direct *P* and *S* waves for both fast and slow components, as well as the SWS δt. In addition, we group the earthquakes into different clusters based on their locations and waveform similarities, and confirm that the obtained variations in the TDs are relatively insensitive to earthquake locations, and mostly reflect temporal changes of material properties in the top 200-m of the crust.

In the following sections, we first describe the analyzed data and background information. In sections 3 and 4, we outline the analysis procedure, and apply it to the entire data set and different groups according to their locations and waveform similarities. We also discuss the observed temporal changes before, during, and after the occurrence of Chia-Yi earthquake. Finally, we compare our results with previous studies and offer possible mechanisms that would explain our observations.

CHAPTER 2

DATA AND BACKGROUND INFORMATION

We use three-component seismograms recorded by the 200-m-deep (173 m below sea level) borehole station CHY, which belongs to the Taiwan Central Weather Bureau Seismic Network (CWBSN). This network consists of 75 stations with S-13 1-Hz short-period velocity seismometers (Shin & Teng 2001). In addition, a free-field strong-motion station CHY073 is co-located with the borehole station, which belongs to the Taiwan Strong-Motion Instrumentation Program (TSMIP). In this study, we only analyze the weak-motion short-period seismic data recorded by the borehole seismometer CHY.

The site CHY is located at a flat plane outside the Chia-Yi city (Figure 1) on the southwestern foothills of Taiwan (Hung *et al*. 1999). Downhole drilling sample shows that the top 30 m contains mixture layer with silty sand and clays (Tai-Tech 2000). The average *S*-wave velocity in the top 30 m is ~200 m/s (http://geo.ncree.org.tw/). This site is classified with class D according to the 1997 UBC Provisions (Kuo 1994; Lee *et al.* 2001; Chung 2006). However, the drilling sample between 30 and 200 m in this site is not available. Therefore, we examine samples from two nearby hydrogeological drilling holes (i.e. squares as shown in Figure 1) within 6 km from CHY from the Hydrogeology Data Bank by the Central Geological Survey of Taiwan (http://hydro.moeacgs.gov.tw/, in Chinese). The core samples show that the top 200 m of the crust around CHY mainly consists of fine- (0.125-0.25 mm) to coarse-grained (0.5-1.0 mm) sandstones, and fine siltstones (0.004-0.063 mm) and mudstones (Liu *et al.* 2005b).

The 10/22/1999 M6.4 Chia-Yi earthquake occurred about one month after the 09/20/1999 Mw7.6 Chi-Chi earthquake (Wen *et. al*. 2007; Chen *et. al*. 2008). The main shock was located

directly beneath the station CHY with a focal depth of 12 km, and was south of the Chelungpu fault (CLF) that ruptured during the Chi-Chi earthquake. The Chia-Yi earthquake was followed by a rigorous aftershock sequence, including one with M6.0 occurred 52 minutes after the main shock. The aftershocks outlined a blind-thrust fault that is dipping to the west from 10-16 km depth (Chen *et al.* 2008).

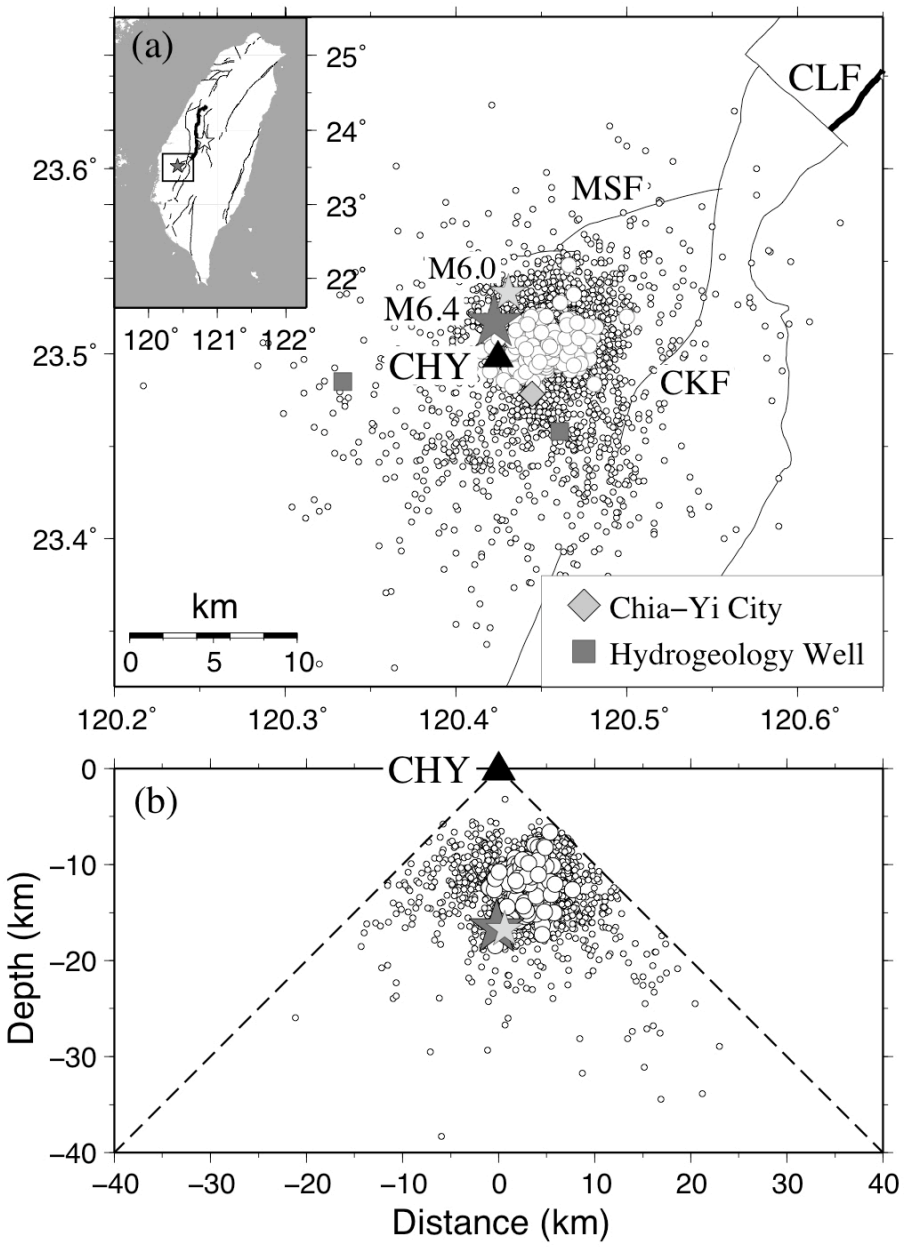

Figure 1. (a) The study area in central Taiwan. The black triangle marks the location of the 200-m-deep borehole station CHY, located at the outside of the Chia-Yi city (the diamond mark). The large star denotes the epicenter of the 10/22/1999 M6.4 Chia-Yi earthquake, and the small star shows the epicenter of the largest M6.0 aftershock. The small circles mark the epicenter of earthquakes with straight-line incident angle less than 45 degrees. The large circles mark the locations of earthquakes belong with similar clusters with $\beta_c \geq 0.85$. The thin lines are the active faults, including Meishan fault (MSF) and Chukou fault (CKF) near Chia-Yi city. Two hydrogeological wells are marked as dark squares. **(b)** The cross-section view below CHY. The inset shows the map of Taiwan with the box correponding to the study area. The white star marks the epicenter of the 09/20/1999 Mw7.6 Chi-Chi earthquake and the bold line is the Chelungpu fault (CLF) ruptured during the Chi-Chi main shock.

CHAPTER 3

ANALYSIS PROCEDURE

We select a total of ~2500 local earthquakes that occurred between March 1991 and March 2002 and are within the shear-wave window of station CHY for further analysis (Nuttli 1961; Cochran *et al.* 2003; Peng & Ben-Zion 2004). The shear wave window is defined as epicentral distances to station CHY less than their hypocentral depths (i.e. straight-line incident angle $\leq$ 45 degrees). We manually pick the arrival times of *P*- and *S*-waves for all events, and only keep those with clear incident and surface reflect waves in three (N, E, and Z) components (e.g. Figure 2). Next, we cut the data 8 s before and 12 s after the *S*-wave arrival, remove the mean value, re-sample the data from 50 to 100 samples/s, and apply a 1 Hz high-passed filter to reduce the long-period background noise. We further eliminate bad quality events according to their signal to noise ratio (*SNR*). The signal window is between 0.5 s before and 1.5 s after the *P*-wave or *S*-wave arrival, and the noise window starts from 2.5 s to 0.5 s before *P*-wave arrival. Any events with $SNR \leq 2.0$ for any of the three components are not used for further analysis (~22% of original events).

Figure 2a shows an example of typical waveforms recorded by the borehole station CHY, which contain several interesting features. First, the *P*- and *S*-waves are most clearly shown in the vertical and two horizontal components, respectively, indicating a near-vertical incidence for the seismic waves. Secondly, clear surface reflected waves are observed on all three components with different time lags, corresponding to different travel times in the top 200 m. Finally, the *S*-wave on the E component arrives about 0.16 s faster than that on the N component, indicating the presence of near-surface anisotropy in this area. Liu *et al.* (2004) measured SWS parameters

in the same region, and found an average delay time δt of 0.16 s and a fast direction φ of 170.2^o $\pm$4.1^o (i.e., CCW from East) from the borehole station CHY, and δt = 0.20 s, φ = 177.5^o $\pm$4.3^o from the surface station CHY073. Their results are generally consistent with the example shown here. We also measured the fast polarization directions for selected events and obtained similar directions. Because the fast direction is near E-W, and the obtained results remain essentially the same before and after rotating to the fast directions, we use waveforms recorded on the E component to represent the quasi-*S* waves corresponding to the fast direction in the following work.

Next, we compute the auto-correlations functions (ACF) for each of the three-component seismograms (Liu *et al.* 2004, 2005b), and measured the TD between the incoming and surface-reflected waves from the zero-lag and secondary peaks in the ACF (Figure 2b). The underlying assumption is that for near-vertical incidence, the ACFs of the surface-reflected waves represent the Green's function for near-surface layers (e.g. Claerbout 1968; Daneshvar *et al.* 1995). This assumption is generally valid for small incident angles because seismic rays tend to bend toward near vertical, due to a reduction in seismic velocities in the near surface layers. In this case, the secondary peaks in the ACF measure the two-way travel times between the surface and the borehole station.

In details, we cut the horizontal component data 1 s before and 3 s after the *S*-wave arrivals, and vertical component data 0.5 s before and 1 s after the *P*-wave arrivals. The time window is chosen to be long enough to include the both the direct and surface reflected waves (~ 0.94 to 1 s TD for the *S*-wave, and ~0.22 s for the *P*-wave), but short enough so that they do not contain both the direct *P* and *S* waves. Then we measure the TD for the up-going and down-going *P*-waves on the vertical component (Z), and *S*-wave for the two horizontal components (N

and E) from secondary peaks in the ACF. As shown in Figure 2b, the maximum peak is at zero lag and the secondary peak corresponds to the TD between the direct and surface-reflected phases. The ratio between the secondary and zero-lag peaks gives the cross-correlation coefficient between the direct and surface-reflected phases. We require that the ratio to be larger than 0.20 to ensure waveform similarity and reliability of the TD. This criterion results in additional dropping of 14% of the data. Finally, we have a total of 1612 (~64% of original events) high-quality events for further analysis. Out of them, 218 events occurred before, and the rest 1394 events occurred after the Chia-Yi earthquake.

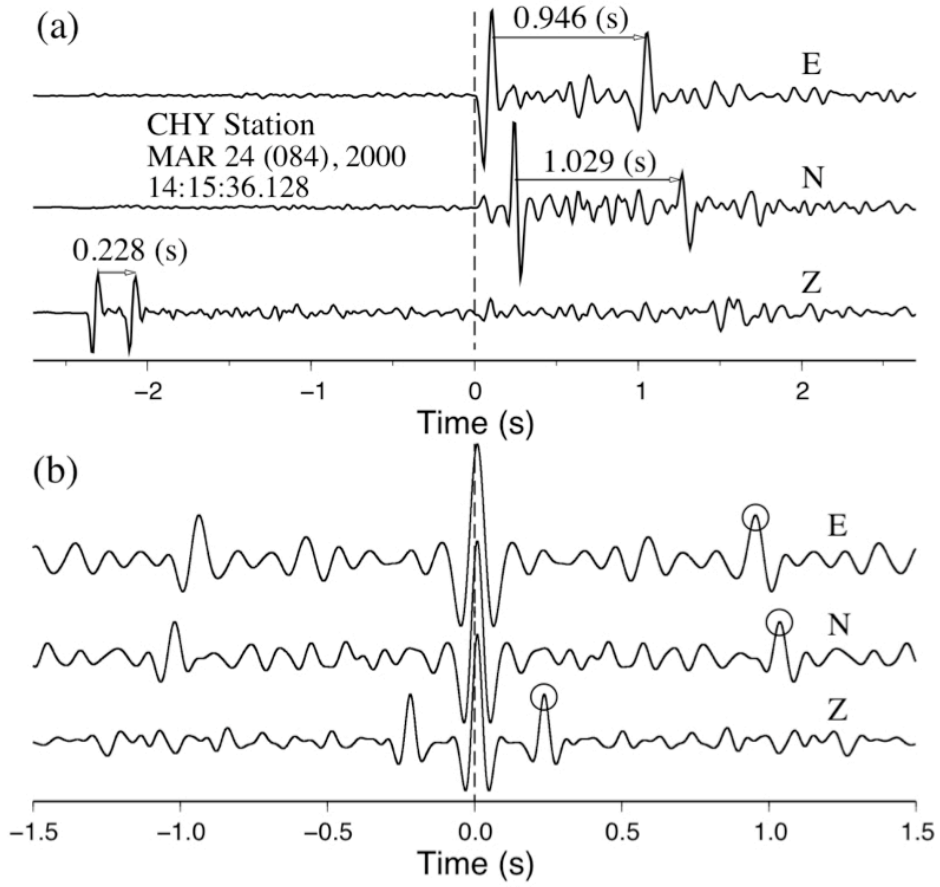

Figure 2. (a) An example of three-component seismograms showing the surface reflected waves and shear wave anisotropy. **(b)** The auto-correlation functions for the three-component seismograms. The dashed line corresponds to zero lag time and the open circles mark the secondary peaks (i.e. two way travel times in the top 200 m.

CHAPTER 4

RESULTS

4.1 General Features

The TDs calculated from three-component seismograms for all 1612 events are shown in Figure 3. The average TD between 1993 and 2002 is 0.944±0.010 s in the E, 1.023±0.010 s in the N, and 0.222±0.007 s in the Z component, respectively. We also compute the average time difference between the N and E components, which is used the as a proxy for SWS delay time δt in the top 200 m. The obtain value is 0.079±0.007 s, which is close to the two-way SWS δt of 0.08 s measured by Liu *et al.* (2004). Other general patterns include: (1) a clear increase of TD for the N and E components at the time of Chia-Yi main shock, followed by a logarithmic-type recovery; (2) a gradual increase of TD for the E and N components in the past 7 years before the main shock; and (3) a lack of clear temporal changes for the differences of TDs between the N and E components (i.e. SWS δt) and the TD for the vertical components.

To further quantify the temporal changes in each component, especially during the co- and post-seismic period, we fit the TD versus logarithmic times since the main shock by a least-squares method, and compute the correlation coefficients (CC) between them. The obtained slopes and the CC values for each component are shown in Figure 3. We also compute the probability of occurrence by chance for each component. If the two-tailed probability is 0.05 (i.e. p=0.05), the occurrence by chance is 5% or the results are significant at the 95% level. The statistical test confirms that the observed correlations for the N, E, and Z components are statistically significant (with <0.05% of occurrence by chance), but the correlation for the SWS δt is not (with 6.5% of occurrence by chance).

The general patterns shown in Figure 3 are observed using all earthquakes within the shear wave window. However, the obtained temporal changes could be affected by mixing the spatial variations with the underlying temporal changes (e.g. Liu *et al*. 2004, 2005b; Peng *et al*. 2005). To examine this further, we plot in Figure 4(a-d) the TDs for the E component versus several earthquake location parameters (e.g. event depth, epicentral distance, apparent incident angle, and back azimuth). The value of apparent incident angle is calculated from the arctangent functions of epicenter distance divided by depth. The true incident angle at station CHY is probably much smaller than the apparent value because the ray tends to bend toward near vertical due to a reduction in seismic velocities in the near surface. A proper calculation of the true incident angle requires accurate knowledge of the hypocenters and 3D velocity model in this region, and hence is not performed here. We use instead the apparent incident angle as a proxy (and upper bound) of the true incident angle and investigate the relationship between the TD and spatial variations.

As shown in Figures 1 and 4a, most of the events (99.4%) are located at 5 to 20 km depth. The depth (CC=0.17) and the back azimuth (CC=–0.24) appear to be less correlated with the TD (with 6.28% and 13.47% of occurrence by chance, respectively). However, the TD shows clear negative correlation with the increasing epicentral distance (CC=–0.44) and incident angle (CC=–0.49), with <0.05% of occurrence by chance. This is mainly because for a homogenous medium, the total separation distances between the up-going and surface reflected waves $\Delta s = 2d\cos i$, where d is the layer thickness, and i is the incident angle (see Appendix A for detailed mathematic deviation). Hence, the separation distances and the travel times between the up-going and surface reflected waves become smaller with increasing incident angles. Finally, the time evolutions of epicentral distances and apparent incident angles for all the earthquakes

(Figure 4e-h) show a similar abrupt co-seismic changes and post-seismic recovery as compared with those in Figure 3. These results suggest that using earthquakes at different locations could potentially cause apparent temporal changes in the TDs. In the next two subsections, we will apply different techniques to group earthquakes into small clusters to reduce the effects of spatial variations on temporal changes.

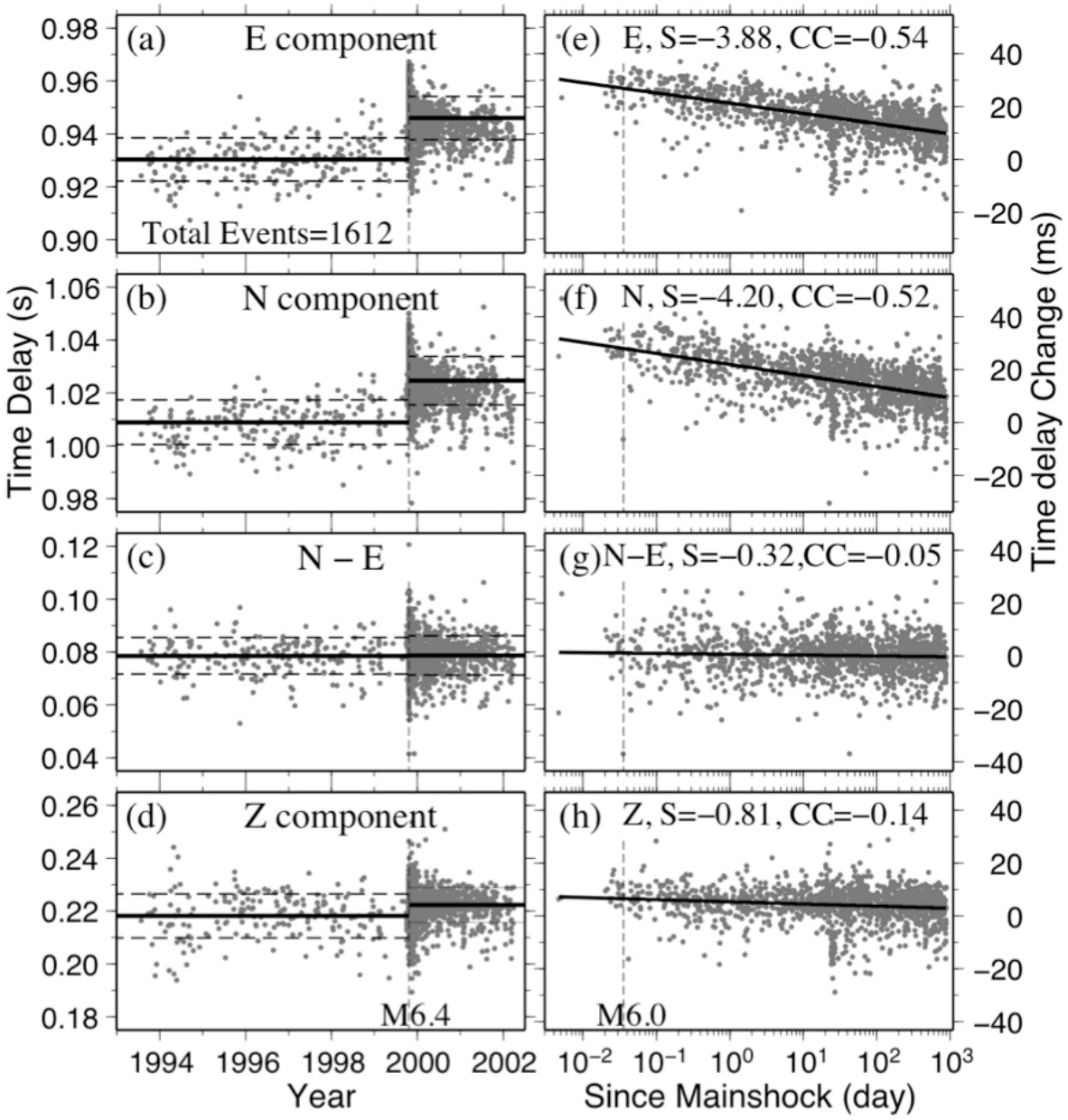

Figure 3. (a-d) Temporal changes of time delays (TDs) for the E, N, N−E, and Z components versus the occurrence times of all 1612 events analyzed in this study. The solid lines represent the mean TD before and after M6.4 Chia-Yi earthquake, and the standard deviations are marked as dotted lines. **(e-h)** Temporal changes of TD for all components plotted with logarithmic time (in days) since the Chia-Yi main shock. The solid line marks the least-squares fitting of the data. The vertical dashed line mark the occurrence of the M6.0 aftershock. The measured slope S (ms per decade change in time), and the correlation coefficient (CC) values are also shown on the top of each panel.

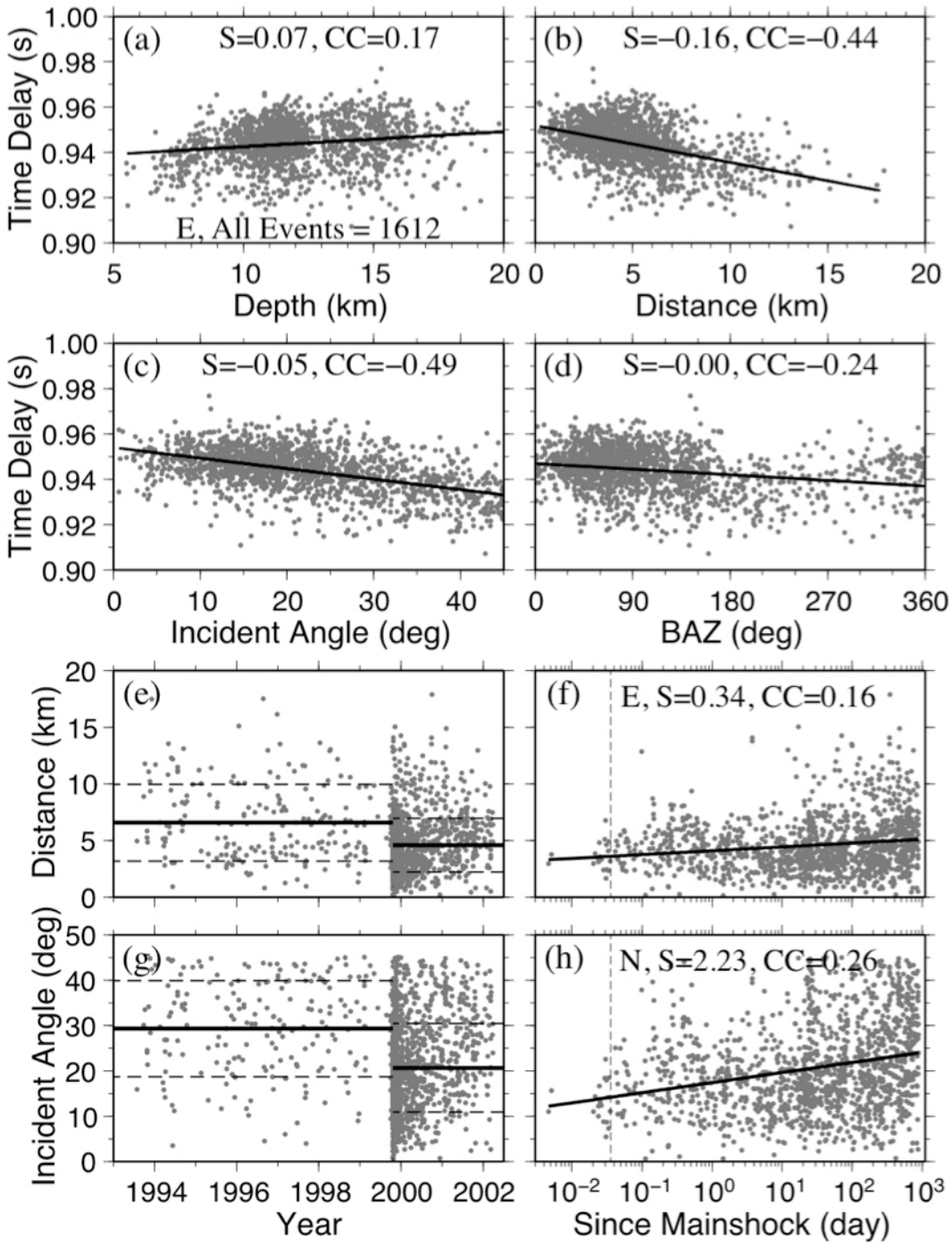

Figure 4. The TDs measured on the E component versus event depth **(a)**, epicentral distance **(b)**, apparent incident angle **(c)**, and back azimuth **(d)** for all 1612 events. The epicentral distance versus the occurrence time **(e)** and logarithmic time since the Chia-Yi mainshock **(f)**. The apparent incident angle versus the occurrence time **(g)** and logarithmic time since the Chia-Yi mainshock **(h)**. Other symbols and notations are the same as in Figure 3.

4.2 Grouping by Earthquake Locations

First, we use 259 earthquakes that are within 3 km in radius to CHY and 10 to 15 km in depth. Figure 5 shows the observed TDs for different components versus the logarithmic time after the main shock. The general patterns are similar to Figure 3, and the scatters are somewhat reduced. In addition, because we only select earthquakes directly beneath station CHY, the apparent incident angles do not show significant dependence with TDs. The results from using 1 to 2 km radius show similar patterns, although the numbers of events are reduced to 22, and 108, respectively.

Next, we group the 1612 events into small cube cells with 5 km in length and examine the TDs within each cube separately. We choose 5 km mainly based on the location error of the CWB catalog, which is about 4 km in the study region (Wu & Teng 2002). It also reflects a tradeoff between the need of small cube cells to remove spatial variations, and the need to have enough events for better statistic. We require that each group should contain at least 20 events and the time period is long enough to span from one day to 2 year after the main shock. A total of 11 cube cells between 5 and 20 km in depth, and within 10 km in both E-W and N-S direction have been selected. Figure 6(a-d) show the measured slopes for different groups between the TDs and logarithmic times since the main shock. It is clear that for all groups, the TD measured at the E and N components increase at the time of the main shock and recovery gradually, but virtually no temporal changes are observed for the Z component and the time difference between N and E components (i.e. SWS δt). We also check the dependence on TDs on the apparent incident angle for each of the cube, and find no clear correlation among them (Figure 6e).

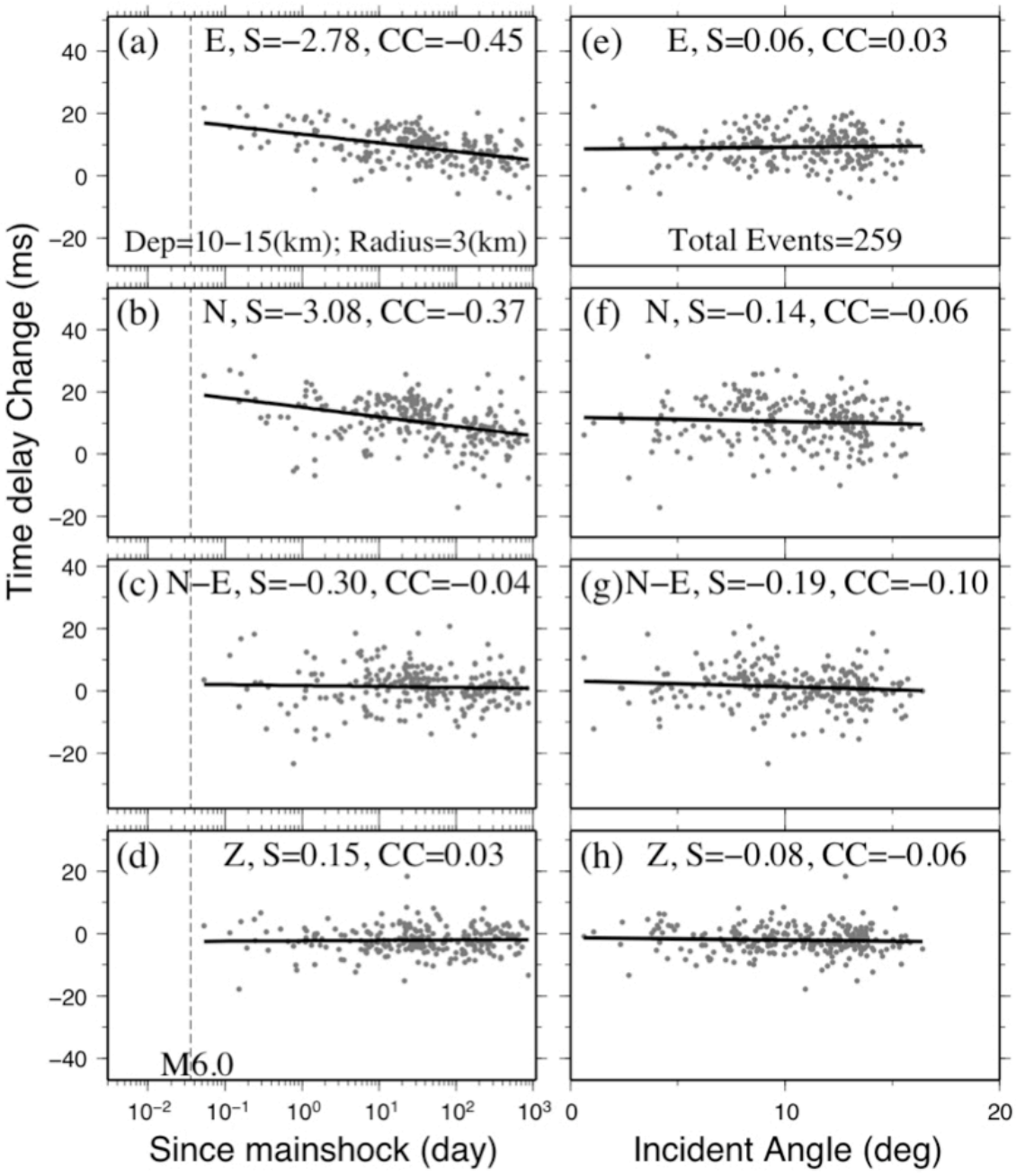

Figure 5. (a-d) Temporal changes of the TDs for all components plotted with logarithmic time (in days) since the Chia-Yi main shock for 248 events within 3 km of station CHY and in the depth of 10−15 km. **(e-h)** The TDs for all components versus the apparent incident angles. Other symbols and notations are the same as in Figure 3.

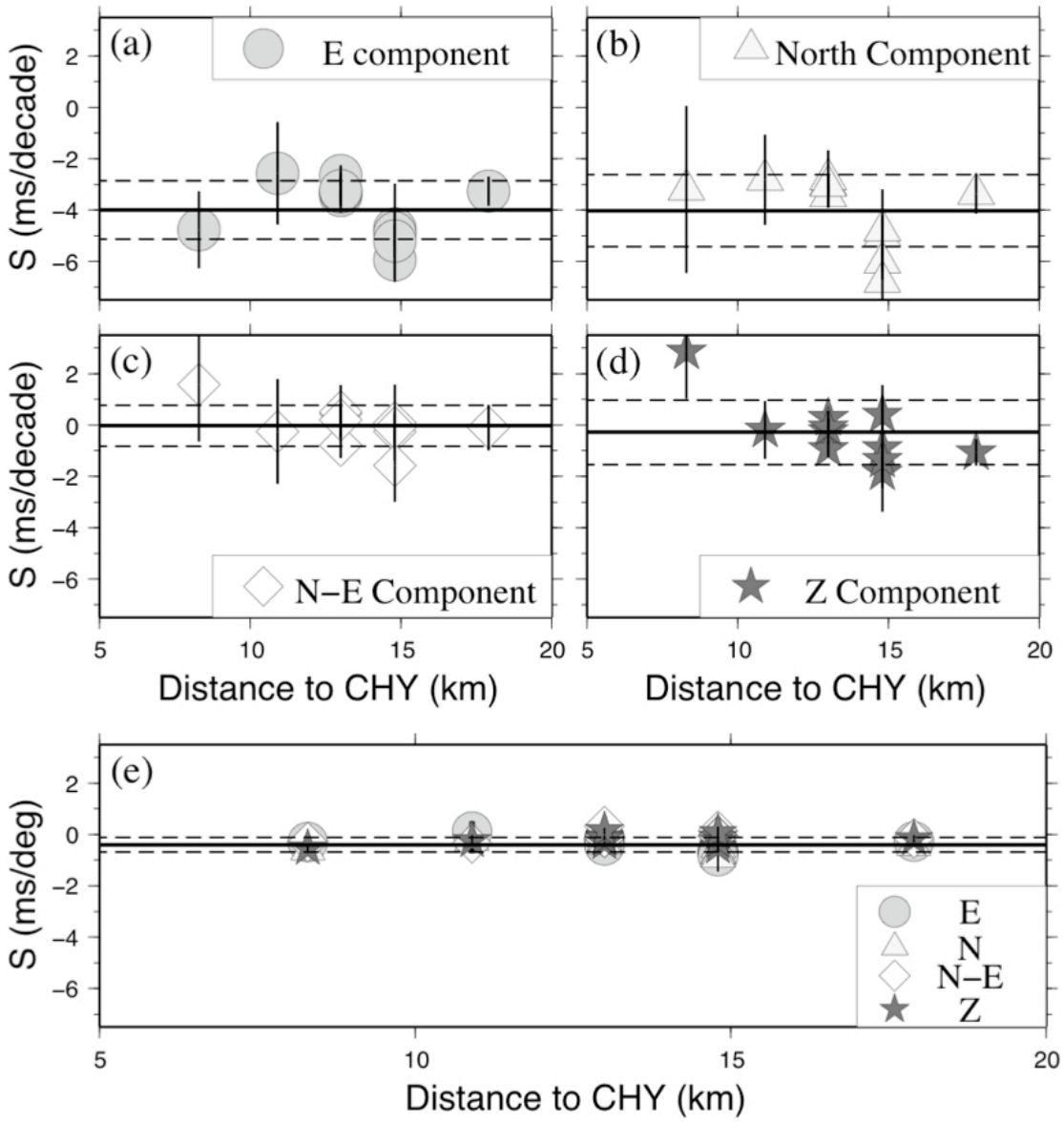

Figure 6. (a-d) The slopes between the TDs and the logarithmic time since the Chia-Yi mainshock for all components measured from 11 groups of earthquakes versus the epicentral distances. The solid line marks the mean slope, and the dashed lines correspond to the one standard deviation of the mean. **(e)** The slopes between the TDs and the apparent incident angles for all components and all 11 groups of earthquakes.

4.3 Grouping by Similar Earthquake Clusters

In the second approach, we group earthquakes into similar earthquake clusters by waveform cross-correlation (Aster & Scott 1993; Peng & Ben-Zion 2005) to minimize the mixing of spatial variations with temporal changes in our seismic data. The underlying assumption is that in a heterogeneous earth structure, only earthquakes in the nearby region generate similar waveforms (Menke & Schaff 2004; Peng & Ben-Zion 2005). In detail, we compute the waveform cross-correlations starting from 2 s before to 3 s after the arrival of *S*-wave in E, N, and Z components. Next, we compute median correlation coefficient (β) between event pairs with inter-hypocentral distance less than 5 km. Finally, we identify pairs of events that satisfy a given similarity criterion ($\beta > \beta_c$) and group such pairs into similar earthquake clusters using an equivalency class (EC) algorithm (e.g. Press *et al.* 1986). The resulting number of clusters and total number of events within each cluster depend on the β_c value (e.g. Peng & Ben-Zion 2005). For example, the number of events in the largest cluster is 684, 340, and 188 with $\beta_c \geq 0.80$, 0.85, and 0.90, respectively.

The obtained temporal changes in TD for the largest cluster with different choice of the β_c value are shown in Figures 7-9. Figure 10 shows the obtained ACF around the secondary peaks for three-component seismograms with $\beta_c \geq 0.85$. Other groups of cluster (e.g., second, third, and fourth largest clusters) with $\beta_c \geq 0.80$ are shown in Appendix B1. The overall patterns are very similar to each other, and are consistent with those shown in Figures 3 and 5. In addition, the correlation between the TD and the earthquake location discussed in Appendix A are largely reduced (Figure 11), and show random distribution in space (Figure Appendix B2).

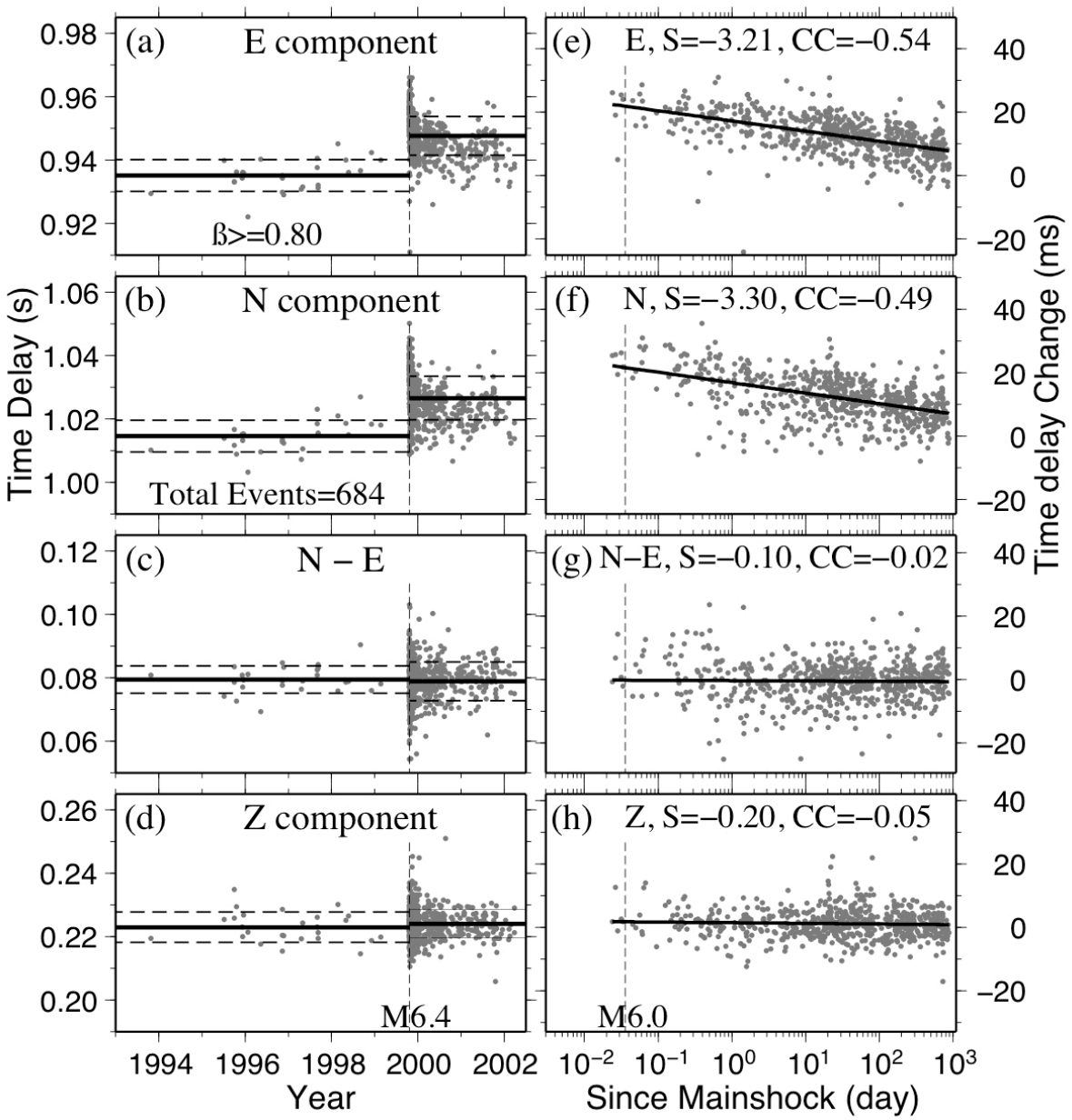

Figure 7. (a-d) Temporal changes of time delays (TDs) for the E, N, N−E, and Z components versus the occurrence times of 684 earthquakes in the largest similar cluster with $\beta c \geq 0.80$. **(e-h)** Temporal changes of TD for all components plotted with logarithmic time (in days) since the Chia-Yi main shock. The probabilities of occurring by chance for the correlation between the TDs and the occurrence times before the mainshock are 2.6% (CC=0.44), 0.2% (CC=0.58), 40.6% (CC=0.17), and 35.8% (CC=–0.18) for E, N, N−E, and Z components, respectively. The probabilities of occurrence by chance for the correlation between the TDs and the logarithmic times since the mainshock are <0.05% (CC=–0.54), <0.05% (CC=–0.49), 67.2% (CC=–0.02), and 24.4% (CC=–0.05) in E, N, N−E, and Z component, respectively. Other symbols and notations are the same as in Figure 3.

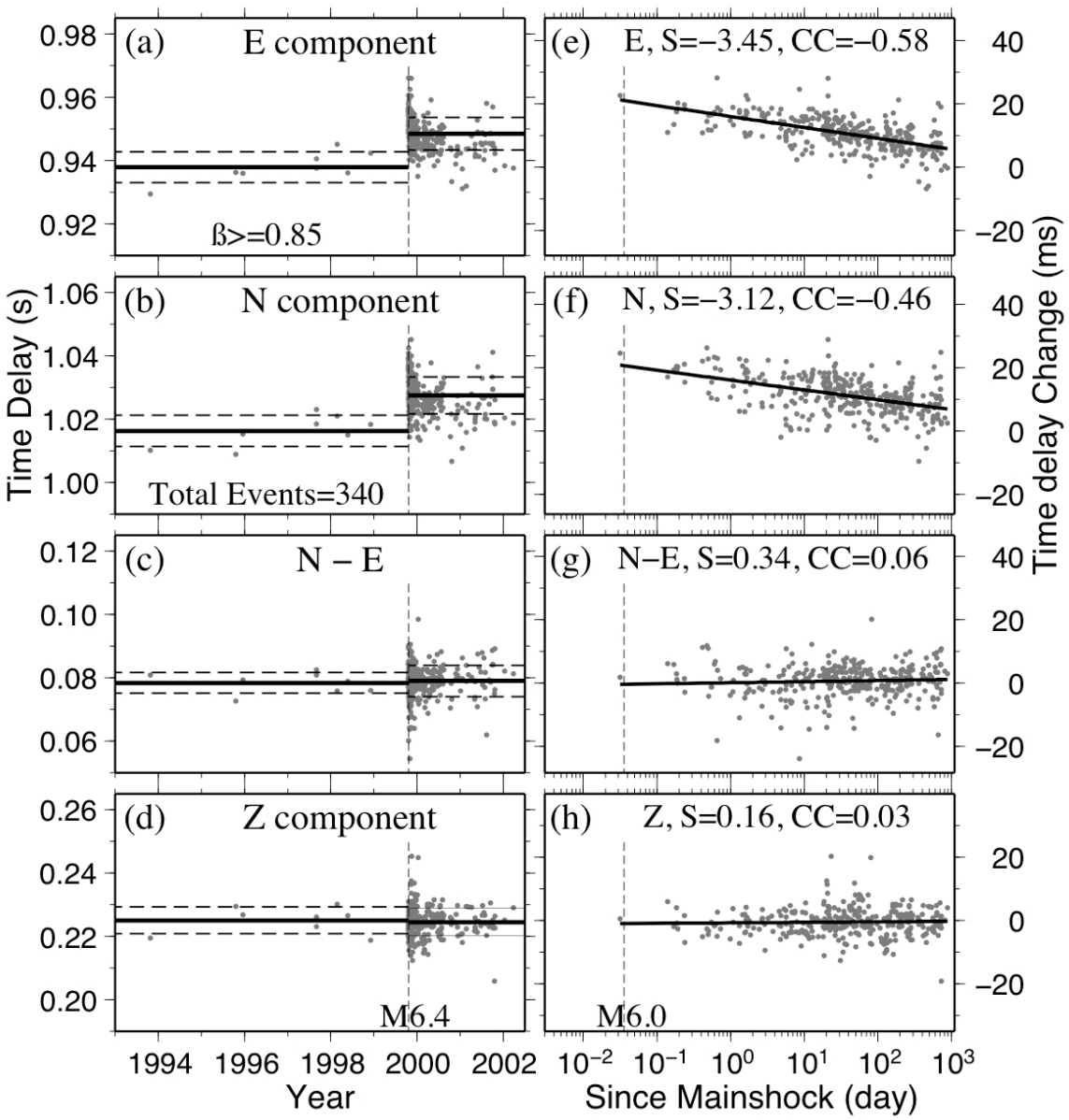

Figure 8. (a-d) Temporal changes of time delays (TDs) for the E, N, N−E, and Z components versus the occurrence times of 340 earthquakes in the largest similar cluster with $\beta c \geq 0.85$. **(e-h)** Temporal changes of TD for all components plotted with logarithmic time (in days) since the Chia-Yi main shock. The probabilities of occurring by chance for the correlation between the TDs and the occurrence times before the mainshock are 1.3% (CC=0.82), 4.2% (CC=0.72), 79.8% (CC=–0.11), and 77.5% (CC=0.12) for E, N, N−E, and Z components, respectively. The probabilities of occurrence by chance for the correlation between the TDs and the logarithmic times since the mainshock are <0.05% (CC=–0.58), <0.05% (CC=–0.46), 28.6% (CC=0.06), and 55.1% (CC=0.03) in E, N, N−E, and Z component, respectively. Other symbols and notations are the same as in Figure 3.

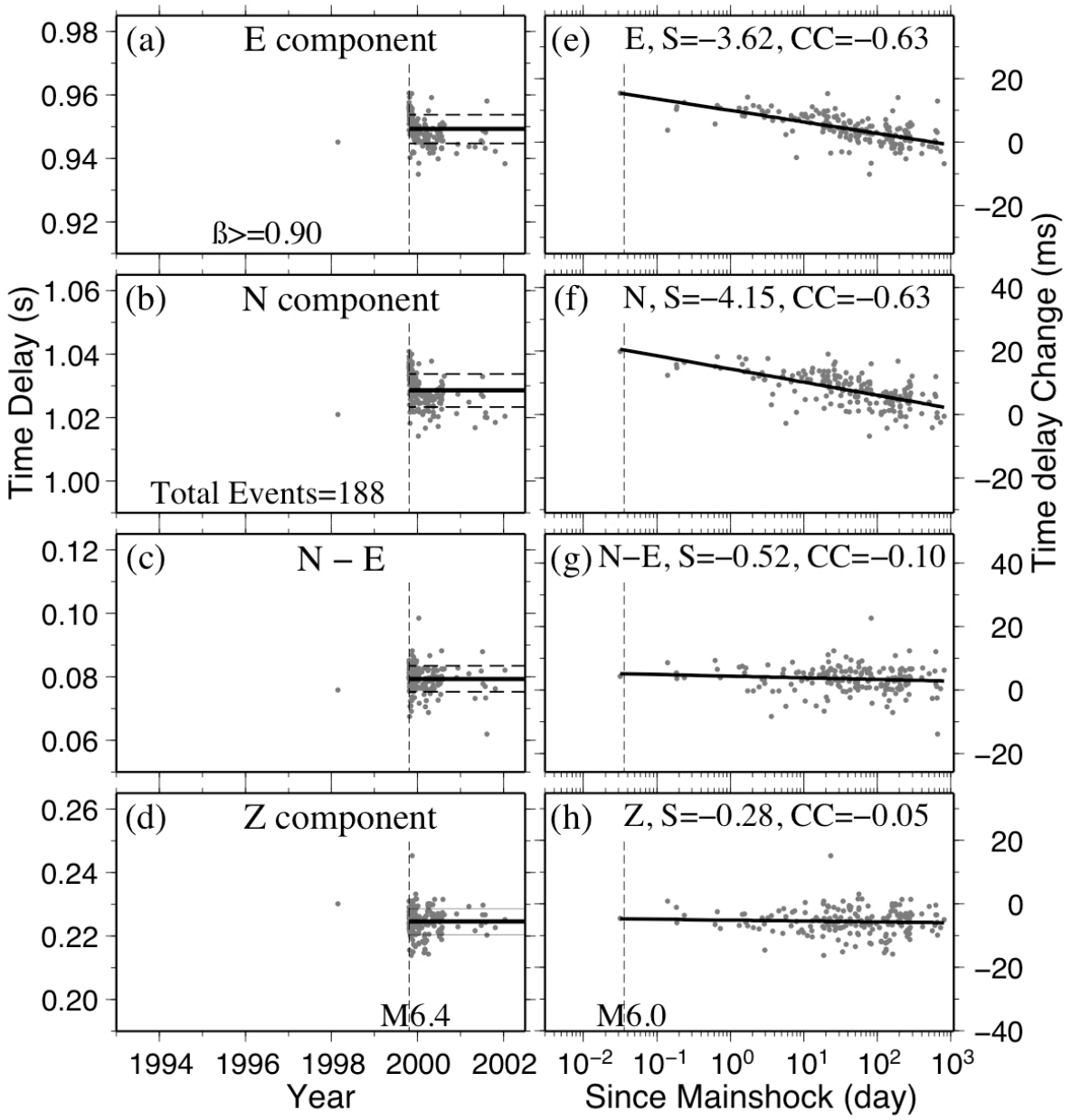

Figure 9. (a-d) Temporal changes of time delays (TDs) for the E, N, N−E, and Z components versus the occurrence times of 180 earthquakes in the largest similar cluster with $\beta c \geq 0.90$. **(e-h)** Temporal changes of TD for all components plotted with logarithmic time (in days) since the Chia-Yi main shock. The probabilities of occurrence by chance between the TDs and the logarithmic time since the mainshock are <0.05% (CC=–0.63), <0.05% (CC=–0.63), 16.6% (CC=–0.10), and 46.5% (CC=–0.05) in E, N, N−E, and Z component, respectively. Other symbols and notations are the same as in Figure 3.

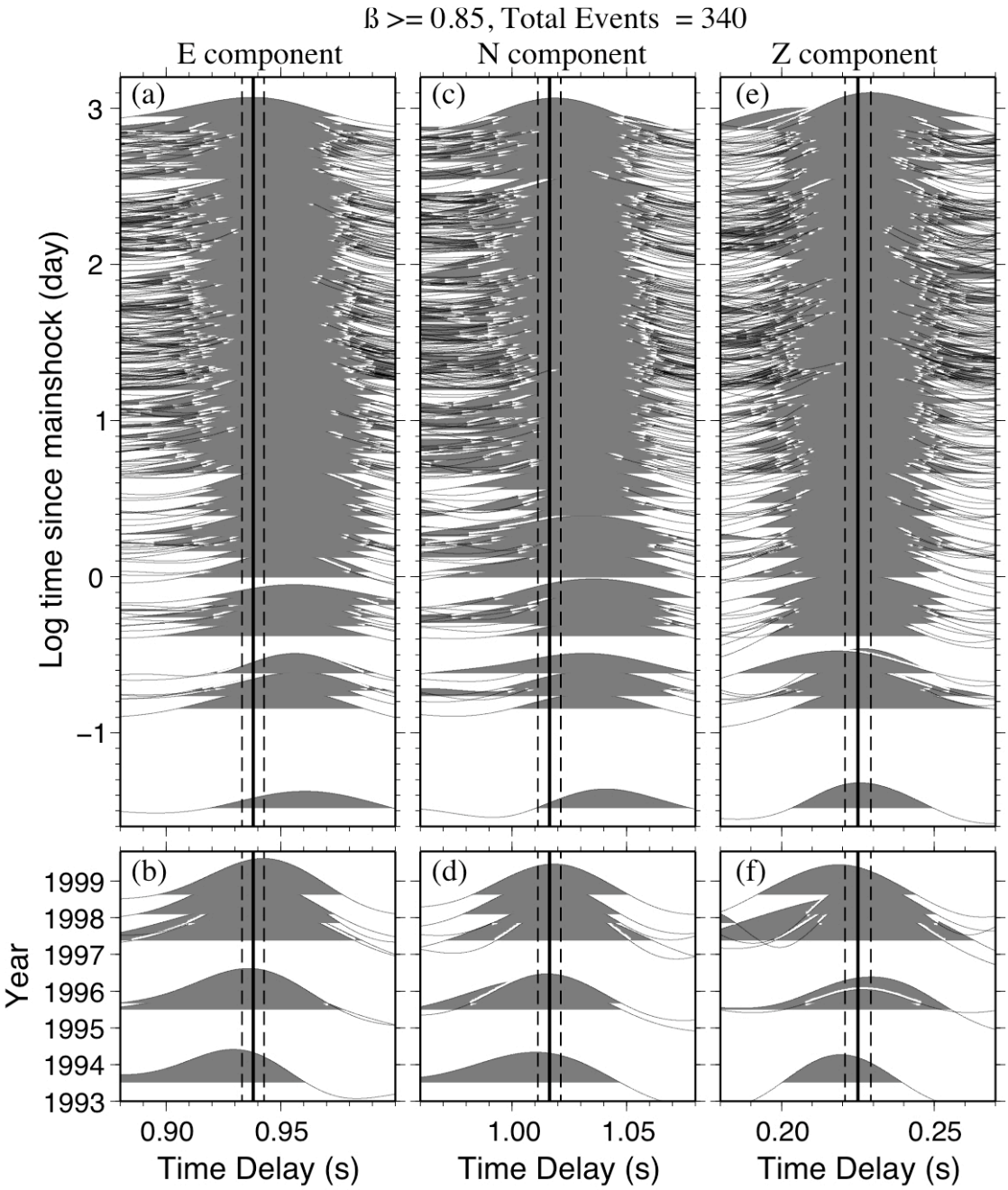

Figure 10. Auto-correlation functions (ACF) in E **(a, b)**, N **(c, d)**, and Z **(e, f)** components for 340 similar earthquakes with $\beta c \geq 0.85$. The lower panel shows the ACF versus the occurrence time before the main shock. The upper panel shows the ACF versus logarithmic time since Chia-Yi main shock. The vertical solid line marks the average TD before the main shock, and the standard deviation are marked as dotted lines (i.e. 0.9379±0.0048 s in E, 1.0163±0.0049 s in N, and 0.2250±0.0042 s in Z). The increasing rate of TD at ~1 hour after the main shock is +1.28% in E, +2.02% in N, and +0.44% in Z.

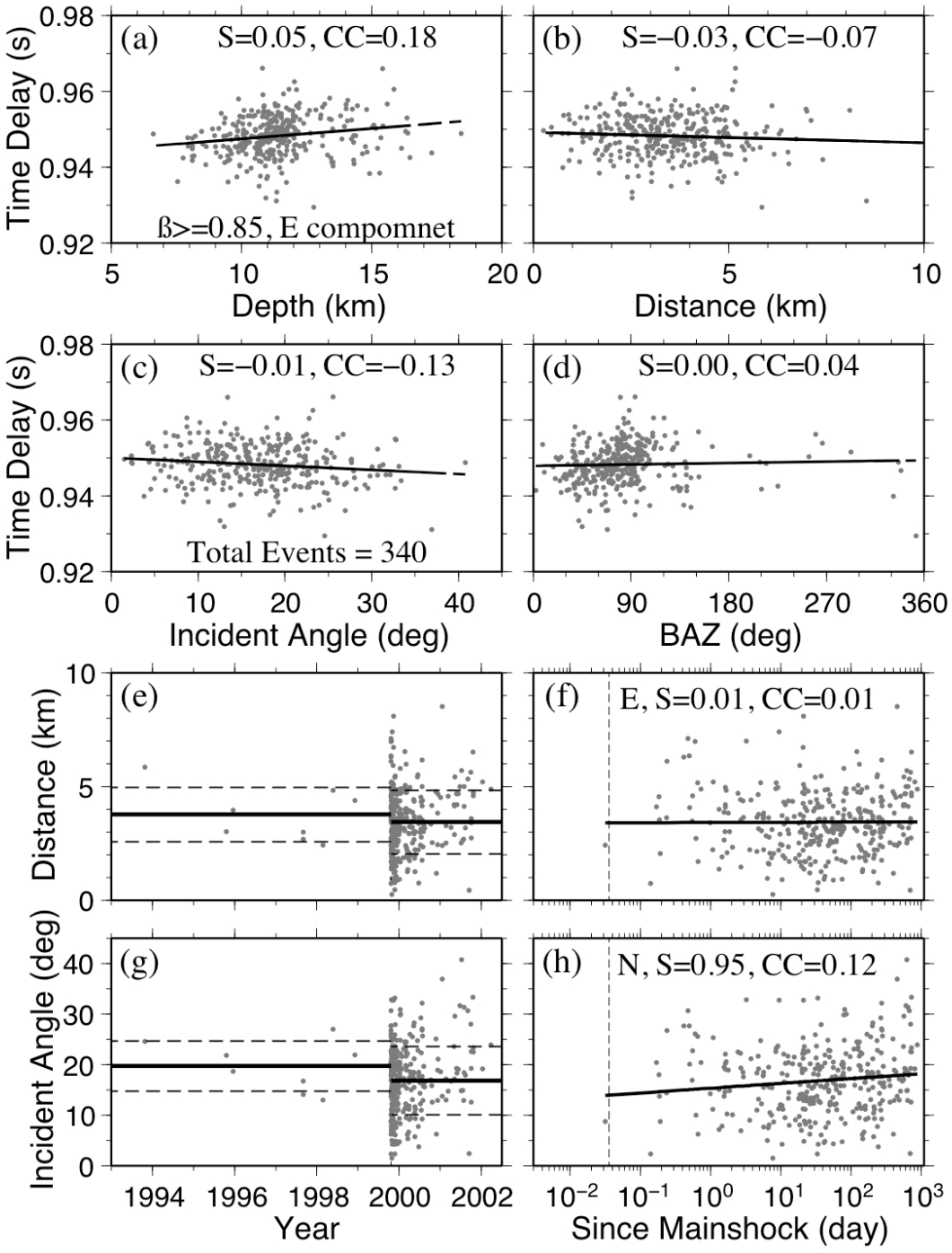

Figure 11. The TDs measured on the E component versus event depth **(a)**, epicentral distance **(b)**, apparent incident angle **(c)**, and back azimuth **(d)** for the 340 similar earthquakes with $\beta c \geq 0.85$. The epicentral distance versus the occurrence time **(e)** and logarithmic time since the Chia-Yi mainshock **(f)**. The apparent incident angle versus the occurrence time **(g)** and logarithmic time since the Chia-Yi mainshock **(h)**. Other symbols and notations are the same as in Figure 4.

4.4 Pre-, Co-, and Post-seismic Temporal Changes

Since the results from different choice of β_c are similar (Figures 7-9), we calculate the co- and post-seismic velocity variations from similar clusters with $\beta_c \geq 0.85$. We compute the average TD for each component and use it as a measure of the level before Chia-Yi main shock. Since the post-seismic changes approximately linear in logarithmic time, we fit the data by a least-squares procedure using a logarithmic relation (Peng & Ben-Zion 2006)

$$TD(t) = a - b\log_{10}(t / day), \quad (1)$$

where a is the TD in ms at 1 day after the main shock, b is a measure of the decreasing rate of the TD per decade change in time. The parameter a is associated with initial conditions, while the parameter b represents a healing rate (e.g. Lyakhovsky *et al.* 1997, 2005). We note that this equation is valid for finite positive times because it diverges as t approaches 0 or infinity. The co-seismic change is measured as the difference between the extrapolated TD at 1 hour after the main shock and the averaged TD before the main shock. We choose 1 hour because it is close to the starting time of the measurement after the main shock. The actual co-seismic and early post-seismic changes could be much larger (e.g. Karabulut & Bouchon 2007; Sawazaki *et al.* 2006, 2008; Wu *et al.* 2008), but we do not have valid data point during and immediately after the main shock to provide further constraints. Hence, the co-seismic changes reported below should be considered as lower bounds.

As shown in Figure 8, the TDs for the E (fast *S*) and N (slow *S*) components increase co-seismically from 0.938 s to 0.950 s and from 1.016 s to 1.037 s, respectively. The TD in the Z component (*P*-wave) drops co-seismically from 0.225 s to 0.224 s. The SWS δt decreases co-seismically from 78.35 ms to 77.95 ms. If we assume that the ray paths in the top 200 m of shallow crust remain unchanged before and after the main shock, we can directly convert the

measured TD into travel-time changes in *P* and *S* seismic velocities by dividing the two-way travel distance of 400 m. The obtained *P*, fast and slow *S* waves before the main shock are 1781.6 m/s, 421.8 m/s, and 389.4 m/s, respectively. The magnitude of the SWS (defined as the difference in the speed of fast and slow waves divided by their average) in the top 200 m is 8%. The corresponding co-seismic velocity changes in the fast *S*, slow *S*, *P*, and magnitude of SWS is −1.28%, −2.02%, −0.44%, and +0.51%, respectively. As noted before, the small co-seismic changes in the *P* waves and SWS δt are not statistically significant. The healing rates of TD in E and N component are −3.45 ms and −3.12 ms per decade changes in time after the main shock, respectively. We note that about 27 months (i.e. March 2002) after the main shock, the TD still does not reach to the average value before the main shock, suggesting a relatively long recovery process.

We also examine the data in the previous 7 years before the Chia-Yi main shock, and find a gradual increase of TDs for both the fast and slow *S* waves. Such changes are shown both in the entire data set with relatively large scatters (Figure 12 a-b), and the similar earthquake clusters with relatively small number of observations (Figure 12 e-f). The least-squares fitting to the data with $\beta_c \geq 0.85$ shows that the TD increases 2.29 ms/year and 2.09 ms/year in E and N components, respectively. The changes for SWS δt and the Z components are –0.21 ms/year and 0.3 ms/year, respectively. But their correlation coefficients are very low (i.e., the corresponding CC values are shown in Figure 12) and hence these numbers are not statistically significant.

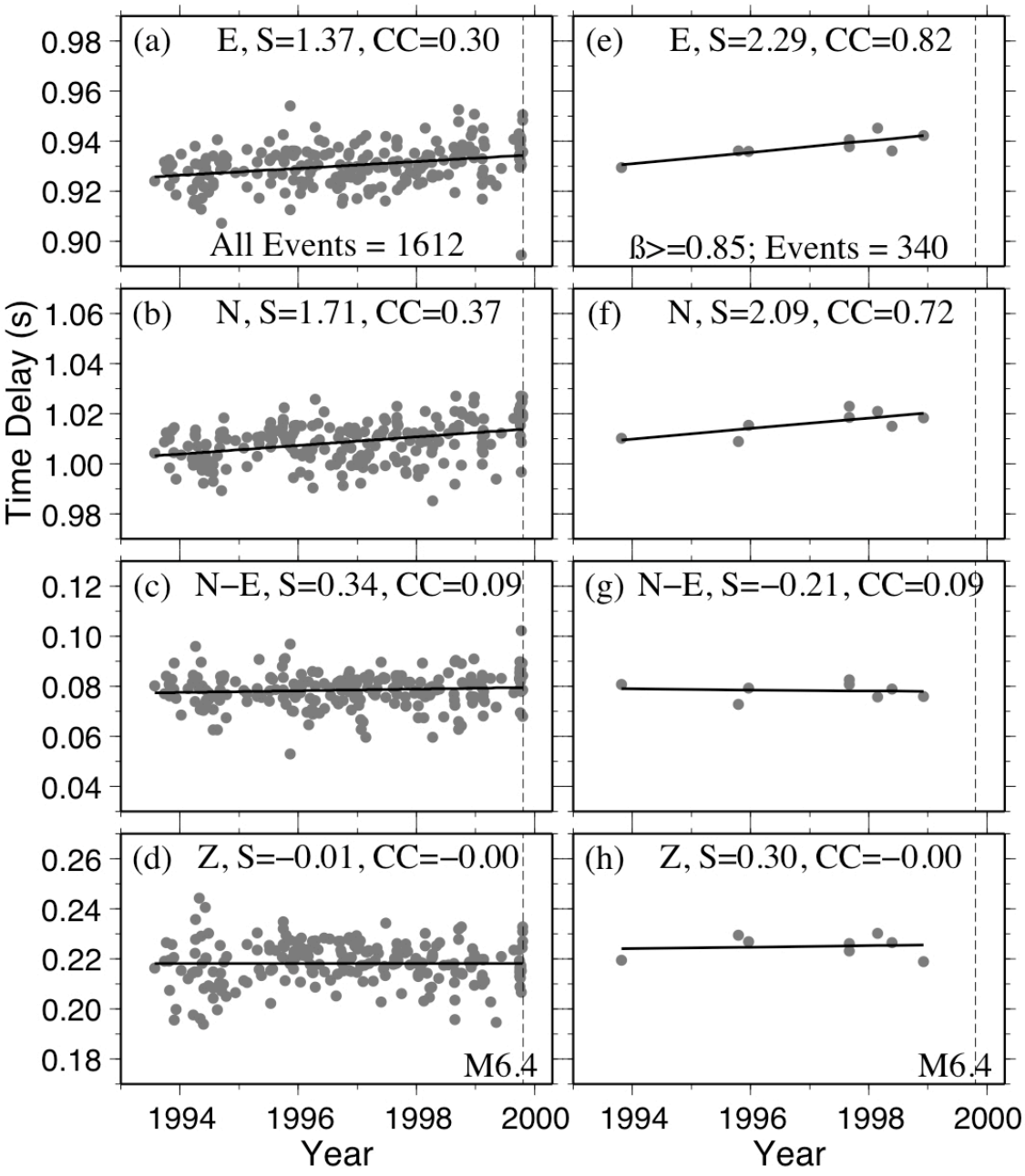

Figure 12. (a-d) Temporal changes of TDs for the E, N, N−E, and Z components versus the occurrence times of all 218 events before the mainshock. The probabilities of occurring by chance for the correlation between the TDs and the occurrence times are <0.05% (CC=0.30), <0.05% (CC=0.37), 19.5% (CC=–0.09), and 98.5% (CC=0.00) for E, N, N−E, and Z components, respectively. **(e-h)** Temporal changes of TDs for the E, N, N−E, and Z components versus the occurrence times of 8 events that belong to the similar clusters with $\beta c \geq 0.85$ before the mainshock. The occurrence by chance is 1.3% (CC=0.82), 4.2% (CC=0.72), 79.8% (CC=0.09), and 77.5% (CC=0.00) in E, N, N minus E, and Z component, respectively.

CHAPTER 5

DISCUSSION

In this study, we utilized surface-reflected *P* and *S* waves to quantify temporal changes of *P*- and *S*-wave velocity, and shear wave anisotropy in the top 200 m of the shallow crust associated with the occurrence of the 1999 M6.4 Chia-Yi earthquake. We found clear co-seismic increases of TD for the *S*-waves on the E (fast) and N (slow) components (on the order of 1-2%), followed by logarithmic recovery. In comparison, the variations for the *P*-wave on the vertical component, and the SWS delay time δt are less than 1%, and not statistically significant.

Several factors can cause the temporal changes observed in this study. These include changing earthquake locations and ray paths, and variations in the elastic properties of the medium. As shown in Figure 4, a systematic decrease of incident angles or epicentral distance could produce an apparent increase of TD observed in this study. However, after grouped the earthquakes into small clusters based on their locations and waveform similarities, we observe similar patterns (Figures 5-10). In addition, the dependences of the observed TDs with earthquake locations are largely reduced (Figures 5 and 11). These results suggest that changing earthquake locations could contribute to the observed scatters, but are not the primary reason for the observed temporal changes. This is perhaps not too surprising because, as mentioned before, seismic rays tend to bend near vertical due to a reduction in seismic velocities in the near surface layers. So the dependence on the ray paths of the incoming waves is rather weak, especially for earthquakes with small epicentral distances (e.g. Figure 5). This is also consistent with the fact that the virtually no *P*-wave energy is shown on the horizontal, and no *S*-wave energy is shown on the vertical components for majority of the events (e.g. Figure 2). Based on these

observations, we suggest that the observed temporal change in the TDs are mainly caused by temporal changes in the medium, rather than caused by spatial variations in the earthquake locations. Because the surface reflected waves only sample the top 200 m of the crust, we attribute the observed temporal changes in TDs to variations of elastic properties in the near-surface layers.

We propose that physical damage in near-surface layers caused by the strong ground motion of nearby large earthquakes is the main cause of the temporal changes in elastic and anisotropic properties observed in this study (Figure 13). Because the fast *S*-wave polarization direction is parallel to the E-W maximum horizontal compressive stress (e.g. Liu *et al.* 2004, 2005a, 2005b), as inferred from the the *P*-axis based on the focal mechanism of Chia-Yi main shock (Chan & Ma 2004), and the regional GPS velocity field (Yu *et al.* 2001), we suggest that preferential alignment of the fluid-filled fractures and microcracks to the direction of the maximum horizontal compressive stress is the main cause of the observed shear wave anisotropy. Fractures with other orientations could also exist but they are likely closed by the E-W maximum horizontal compressive stress. During the Chia-Yi main shock and subsequent large aftershocks, the strong ground motions cause an abrupt increase of crack and void densities, which could be generated by opening and growth of pre-existing fractures and increase of porosity in the shallow surface layers. However, since we observed clear changes in both fast and slow *S*-wave velocities and no resolvble changes in SWS δt, we infer that the coseismic increase of crack and void densities do not have a preferred orientation. In addition, we observed no clear temporal changes in the *P*-wave velocity. Because *S*-wave velocities will change much more than *P*-wave velocities when fluids is present (Mavko *et. al.*, 1998), we suggest that the cracks and void spaces are fluid-filled. This is compatible with a very large *Vp/Vs* ratio of 4.4,

and a Poission's ratio of 0.47 in the study region. After the main shock, the normal stresses would close the co-seismically opened cracks and increase the packing of shallow sediments, resulting in a recovery of seismic velocity to the pre-main shock level in log-linear fashion. Siminar logarithmic healing processes have been observed in laboratory experiments with granular material and rocks under normal stresses (e.g. Dieterich & Kilgore 1996; Marone 1998; TenCate *et al.* 2000; Scholz 2002; Johnson & Jia 2005; Johnson & Sutin 2005). However, due to lack of detailed geological information directly beneath the station CHY, we cannot place a tight constraint on the depth dependence of the co-seismic changes and recovery processes.

Our results are generally consistent with previous studies based on waveform analysis of repeating earthquakes and artifical sources. These studies generally show clear co-seismic reduction of *S*-wave velocities on the order of a few percent in the shallow crust and near active fault zones (e.g. Schaff & Beroza 2004; Peng & Ben-Zion 2006; Rubinstein & Beroza 2004a, 2004b, 2005; Li *et al.* 2006; Rubinstein *et al.* 2007), a smaller changes in *P*-wave velocities (e.g. Schaff & Beroza 2004), and a lack of clear co-seismic changes in shear wave anisotropy (e.g. Peng & Ben-Zion 2005; Liu *et al.* 2004, 2005a, 2008; Cochran *et al.* 2006) associated with large nearby earthquakes. It is worth noting that temporal changes in shear wave splitting of ~0.6% has been observed using the ACROSS (Ikuta & Yamaoka 2004). Such small changes, even if exist, may not be clearly observable using the current tehnique, probably because of mixing of earthquakes with slightly different ray paths. Hence, we suggest that direct measurements of time variations in the direct *S*- and *S*-coda waves, as well as surface reflected *S*-waves, may provide a more promising tool than the shear-wave splitting signals for monitoring temporal changes in the upper crust (Peng & Ben-Zion 2006).

Other recent studies using spectral ratio techniques, which involve comparisons of weak

and strong-motion responses based on the spectral ratio between a target and a reference site, have found much larger (on the order of 20-40 percent) changes in seismic velocities in the shallow crust and inside active fault zones (e.g. Karabulut & Bouchon 2007; Sawazaki *et al.* 2006, 2008; Wu *et al.* 2008a, 2008b). The difference in the observed co-seismic change is mainly caused by the fact that the current work and previous studies of repeating earthquakes are based on waveform analysis of weak motion data, while the spectral ratio technique can be applied to the strong motion data recorded during and in the first few minutes/hours immediately after the main shock, when the recorded weak motion data are mostly off-scale. Hence, the spectral ratio technique can obtain the large co-seismic and very early-postseismic changes that are otherwise not observable by the other techniques.

Nevertheless, all these observations are compatible with the widespread nonlinear site response in the shallow crust during strong ground motion of moderate to large earthquakes (e.g. Beresnev & Wen 1996; Field *et al.* 1997; Rubinstein *et al.* 2004a). Many studies also found that large earthquakes could induce hydrological responses (i.e. changes of water table, surface water flows) and eruptions of volcanoes and geysers at near field and teleseismic distance (e.g. Rojstaczer *et al.* 1995; Brodsky *et al.* 2003; Wang *et al.* 2004; Manga & Brodsky 2006; Elkhoury *et al.* 2006; Manga & Wang 2007; Wang & Chia 2008). For example, Rojstaczer *et al.* (1995) and Wang *et al.* (2004) documented clear increase of streamflows following the occurrence of the 1989 Mw6.9 Loma Prieta and the 1999 Mw7.6 Chi-Chi earthquakes. Rubinstein & Beroza (2004a) suggested that the observed co-seismic increase of streamflow and the decrease of seismic velocity are likely caused by the same mechanism. That is, strong shaking from nearby earthquakes may cause an transient increase of crack density and porosity, which leads to an increase of permeability and streamflows, as well as a reduction of bulk and

shear modulus and the seismic velocity. Recently, Ma (2008) performed 3D dynamic rupture simulations incorporating a yielding criterion in the upper crust. The simulation results suggest that widespread near-surface damages are mainly caused by strong seismic waves, and a 'flower-like' damage zone at depth is mainly induced by dynamic stresses associated with the rupture front, consistent with the field observations.

Finally, we found a gradual increase of TD for both the fast and slow *S*-waves (i.e. decrease of seismic velocities) in the previous 7 years before the Chia-Yi main shock (Figure 12). The underlying mechanism of such pre-seismic changes is still not clear. One posssible mechanism is that the E-W maximum horizontal compressive stress in this region is gradually increasing before the occurrence of the Chi-Chi and Chia-Yi earthquakes, which would result in opening of microcracks preferientally in the E-W direction and an increase of shear wave anisotropy. However, the observed temporal changes in the SWS δt before the main shock are not statistically significant (Figure 12c). Hence, it is more likely that the pre-seismic temporal changes are caused by variations of water table, sediment packing or other surficial processes.

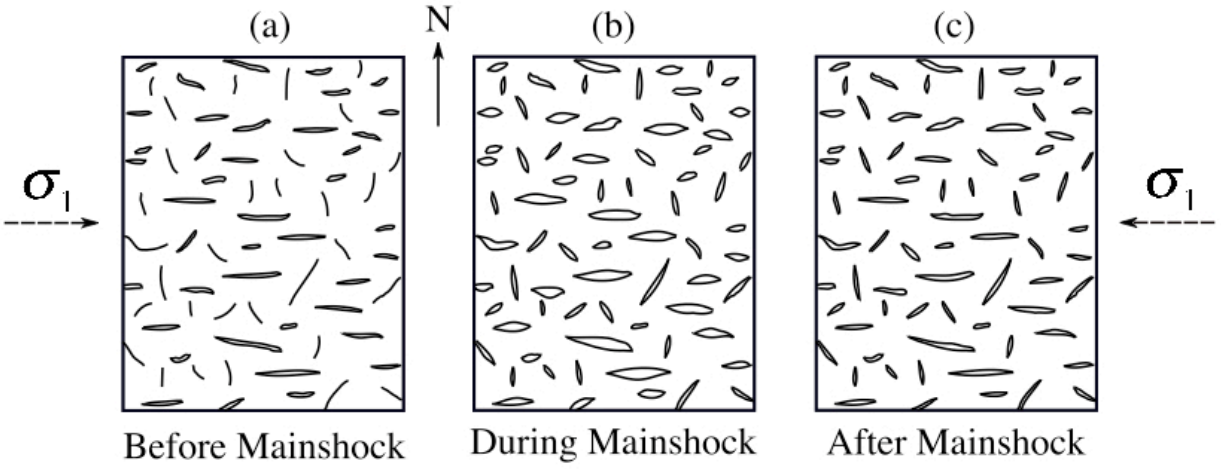

Figure 13. Schematic cartoon demonstrating possible mechanism for the observed temporal changes in the shallow crust before **(a)**, during **(b)**, and after **(c)** the Chia-Yi earthquake.

APPENDIX A

Assuming a homogeneous half space and plane wave incidence, we derive the relationship between the incident angle i the time delays (TD) of up-going and surface reflected waves. The schematic diagram is shown in Figure A1a. For a vertical incidence with $i = 0^o$, the TD is given by

$$\mathrm{TD} = \Delta s/v = 2d/v, \tag{A1}$$

where d is the depth of the borehole seismometer, v is the seismic wave velocity, and Δs is the total propagation distance between the up-going and surface reflected waves.

For a plane wave with incident angle of i, the total propagation distance between the up-going and surface reflected waves can be expressed as

$$\Delta s = DE+EA. \tag{A2}$$

The line segment EA can be expressed in terms of the depth d and the incident angle i as

$$L = EA = EC = d/\cos(i). \tag{A3}$$

The line segment AC can be written as

$$AC = 2{\cdot}AB = 2{\cdot}d\tan(i). \tag{A4}$$

The line segment CD can be expressed in terms of the line segment AC and the incident angle i as

$$\mathrm{CD} = \mathrm{AC}{\cdot}\sin(i) = 2{\cdot}d\tan(i){\cdot}\sin(i). \tag{A5}$$

Hence, the total distance Δs is

$$\Delta s = DE+EA = 2L–CD = 2d/\cos(i)–2d{\cdot}[\sin(i)/\cos(i)]{\cdot}\sin(i) = 2d\cos(i). \tag{A6}$$

So the TD between the up-going and surface reflected waves is

$$\mathrm{TD} = \Delta s/v = 2d\cos(i)/v. \tag{A7}$$

For a vertical incidence with $i = 0^o$, Eq. A7 returns to Eq. A1. If we use the depth of the CHY station d = 200 m, and the fast S wave velocity v = 421.8 m/s before the Chia-Yi main shock, we obtain

$$\mathrm{TD} = 2d\cos(i)/v = 2\cdot 200\cdot\cos(i)/421.8 = 0.9483\cos(i). \quad \text{(A8)}$$

Figure A1b shows the comparison between the predicted TDs (i.e. from equation A8) and observed TDs on the E component (i.e. the same as in Figure 4c) with increasing incident angle i. The predicted TD values fall more rapidly when the incident angle is larger than 10°. This is mainly because the assumption of the homogeneous half-space model. In reality, the seismic velocity is very low in the near surface layers and increases with depth. Hence, the true incident angles could be much smaller than those computed directly using the ratio of the epicentral distance and depth. Using the true (and smaller) incident angles would result in better match between the predicted and observed TDs.

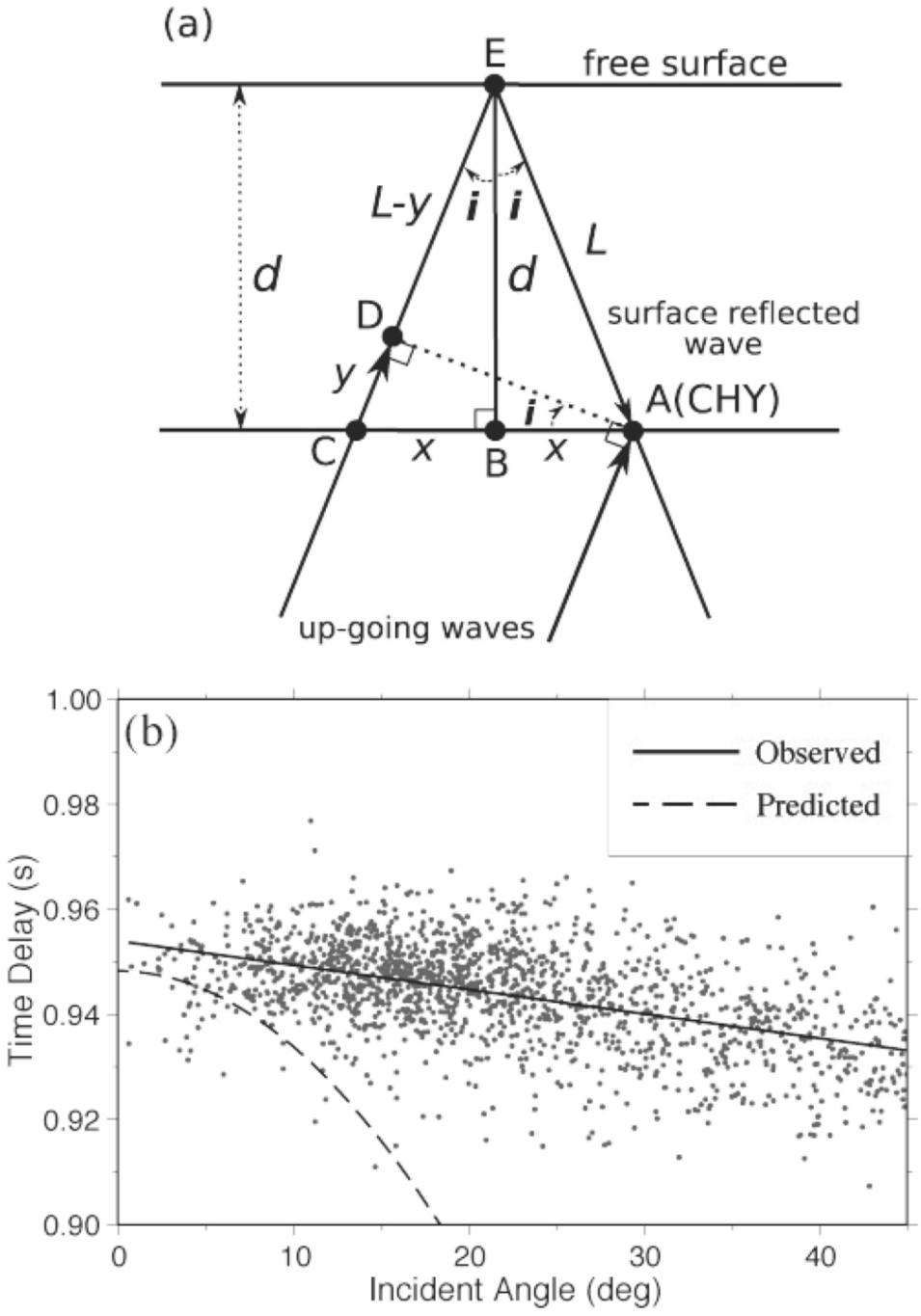

Figure A1. (a) Schematic diagram illustrating the geometry of the up-going and surface reflected waves recorded by a borehole seismometer (at the depth of d) for non-vertical incident waves with an incident angle of i. **(b)** Comparison results between observed and predicted TDs versus incident angles. The observed TDs are measured on the E (fast) component (i.e. the same as shown in Figure 4c). The predicted TD is calculated from the total separation distances between the up-going and surface reflected waves using Eq. A8.

APPENDIX B

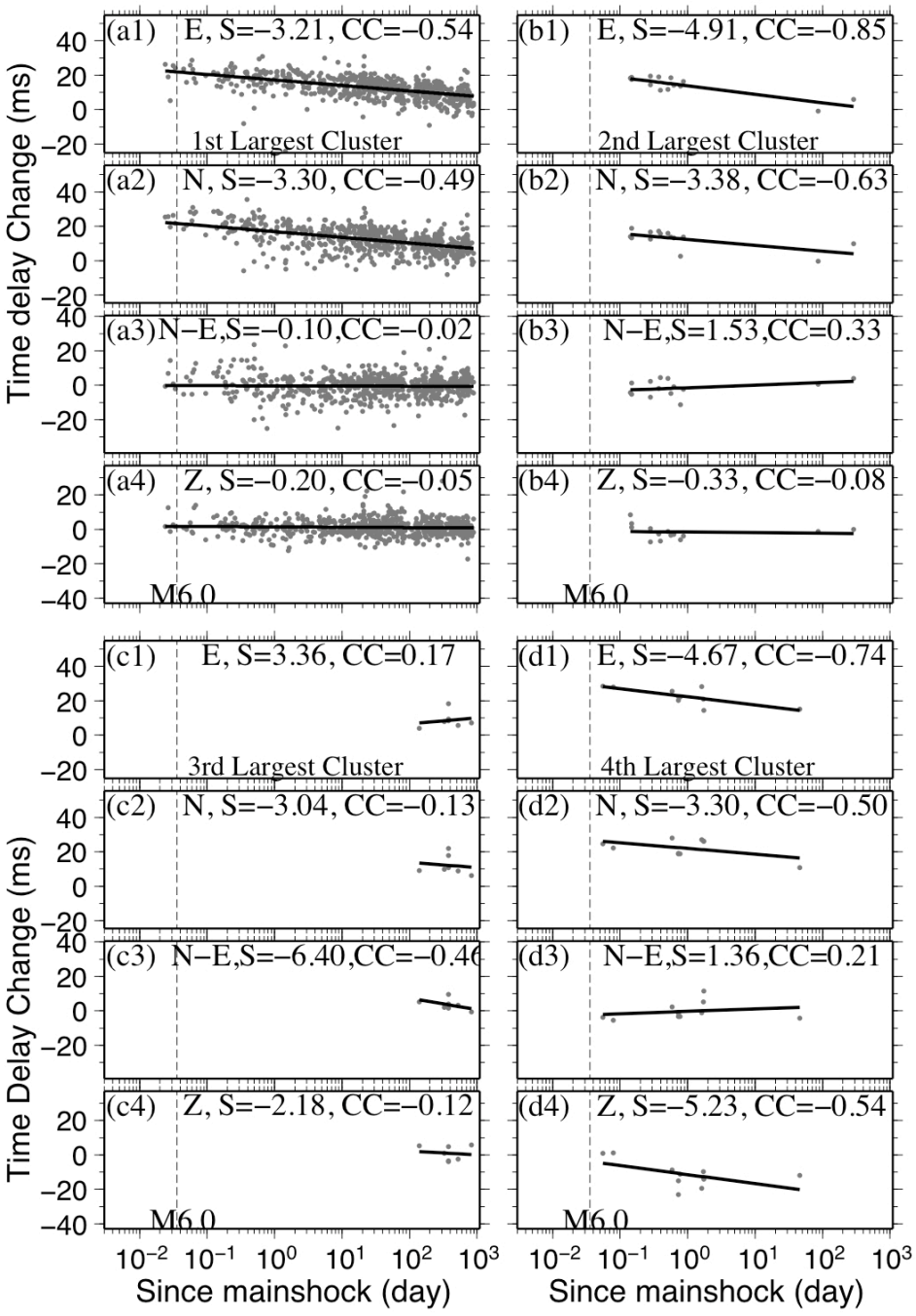

Figure B1. Similar plot as the right panel of Figure 7 **for** the first **(a1-a4)**, second **(b1-b4)**, third **(c1-c4), and** fourth largest clusters **(d1-d4)** with $\beta c \geq 0.80$.

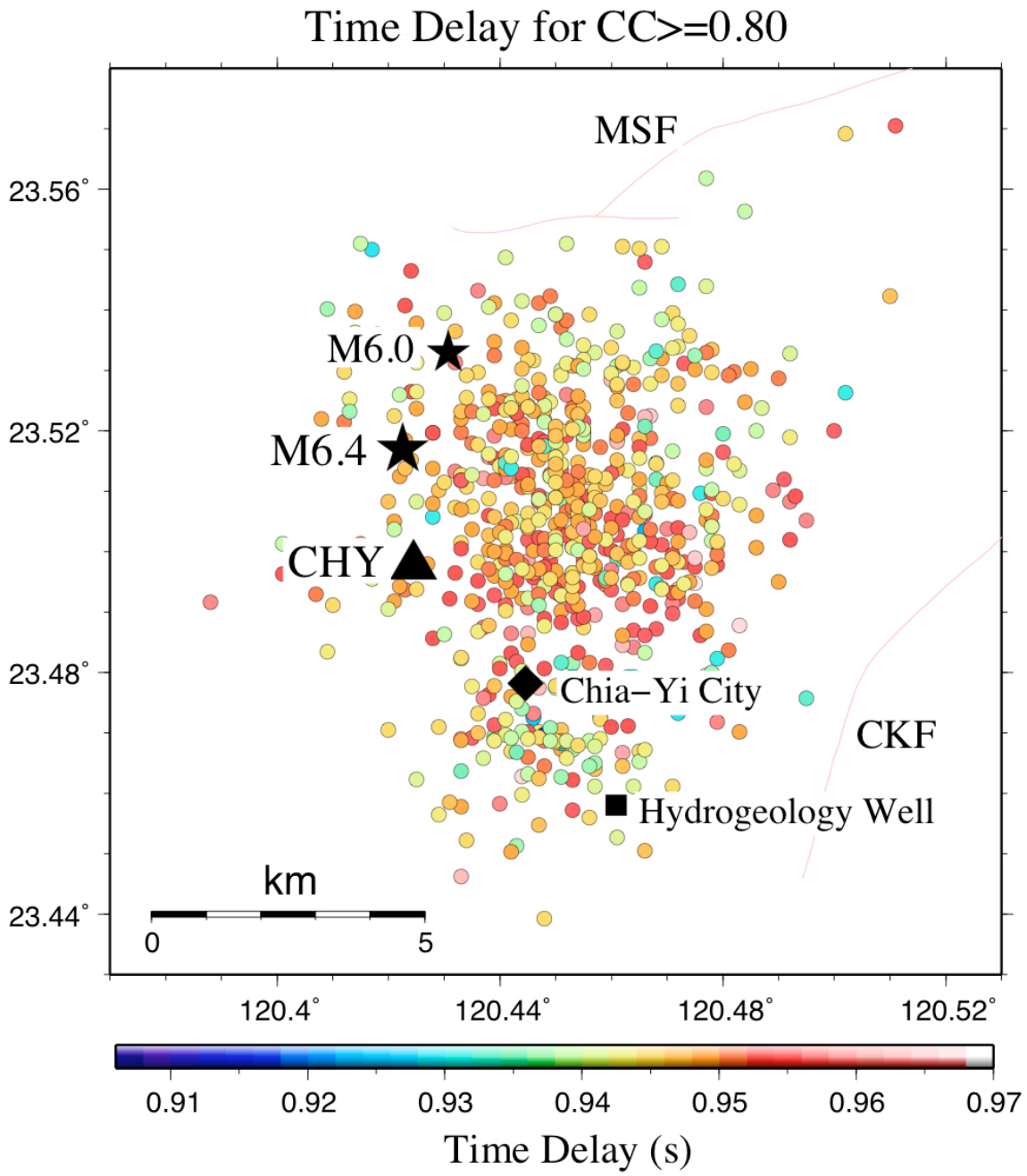

Figure B2. The time delay plot in different colors of event location with $\beta c \geq 0.80$.

REFERENCES

Aster, R.C., Shearer, P.M. & Berger, J., 1990. Quantitative measurements of shear-wave polarizations at the Anza seismic network, southern California: Implications for shear-wave splitting and earthquake prediction, *J. Geophys. Res.*, **95**, 12449–12473.

Aster, R.C. & Shearer, P.M., 1991a. High-frequency borehole seismograms recorded in the San Jacinto Fault Zone, Southern California, Part 1. Polarizations, Bull. Seismol. Soc. Am., 81, 1057–1080.

Aster, R.C. & Shearer, P.M., 1991b. High-frequency borehole seismograms recorded in the San Jacinto Fault Zone, Southern California, Part 2. Attenuation and site effects, Bull. Seismol. Soc. Am., 81, 1081–1100.

Aster, R.C., Shearer, P.M. & Berger, J., 1991. Comments on "Quantitative measurements of shear-wave polarization at the Anza seismic network, Southern California: implications for shear-wave splitting and earthquake prediction by Aster, R.C., Shearer, P.M. & Berger J." – Reply, J. Geophys. Res., 96, 6415–6419.

Aster, R.C. & Scott, J., 1993. Comprehensive characterization of waveform similarity in microearthquake data sets, Bull. Seism. Soc. Am., 83, 1307-1314.

Beresnev, I. A. & Wen, K.-L., 1996. Review: Nonlinear soil response – a reality, Bull. Seism. Soc. Am., 86, 1964-1978.

Beroza, G.C., Cole, A.T. & Ellsworth, W.L., 1995. Stability of coda wave attenuation during the Loma Prieta, California, earthquake sequence, J. Geophys. Res., 100, 3977–3987.

Boness, N. L. & Zoback, M. D., 2004. Stress-induced seismic velocity anisotropy and physical properties in the SAFOD Pilot Hole in Parkfield, CA, Geophys. Res. Lett., 31, L15S17, doi:10.1029/2003GL019020.

Boness, N. L. & Zoback, M. D., 2006. Mapping stress and structurally controlled crustal shear velocity anisotropy in California, Geology, 34(10), 825-828, doi: 10.1130/G22309.1.

Brodsky, E.E., Roeloffs, E., Woodcock, D., Gall, I. & Manga, M., 2003. A mechanism for sustained ground water pressure changes induced by distant earthquakes, J. Geophys. Res., 108, doi:10.1029/2002JB002321.

Chan, C. H. & Ma, K.-F., 2003. Possibility of forecasting aftershock distributions from stress change: a case study of inland Taiwan earthquakes, TAO, 15, 503-521.

Chen, Y.-G., Kuo, Y.-T., Wu, Y.-M., Chen, H.-L., Chang, C.-H., Chen, R.-Y., Lo, P.-W., Ching, K.-E. & Lee, J.-C., 2008. New seismogenic source and deep structures revealed by the 1999 Chia-yi earthquake sequence in southwestern Taiwan, Geophys. J. Int., 172, 1049–1054.

Chung, J.-K., 2006. Prediction of peak ground acceleration in southwestern Taiwan as revealed by analysis of CHY array data, TAO, 17 (1), 139-167.

Claerbout, J. F., 1968. Synthesis of a layered medium from its acoustic transmission Response, Geophysics, 33, 264-269.

Cochran, E. S., Vidale, J. E. & Li, Y.-G., 2003. Near-fault anisotropy following the Hector Mine earthquake, J. Geophys. Res., 108, 2436, doi 10.1029/2002JB002352.

Cochran, E. S., Li, Y.-G. & Vidale, J. E., 2006. Anisotropy in the shallow crust observed around the San Andreas Fault before and after the 2004 M 6.0 Parkfield earthquake, Bull. Seism. Soc. Am., 96(4B), S364-S375.

Coutant O., 1996. Observation of shallow anisotropy on local earthquake records at the Garner Valley, southern California, downhole array, Bull. Seism. Soc. Am., 86(2), 477-488.

Crampin, S., Booth, D.C., Evans, R., Peacock, S. & Fletcher, J.B., 1990. Change in shear-wave splitting at Anza near the time of the North Palm Springs earthquake, J. Geophys. Res., 95, 11197–11212.

Crampin, S., Booth, D.C., Evans, R., Peacock, S. & Fletcher, J.B., 1991. Comment on ‘‘Quantitative measurements of shear-wave polarizations at the Anza seismic network, Southern California: Implications for shear-wave splitting and earthquake prediction’’ by Aster, R.C., Shearer, P.M., and Berger, J., J. Geophys. Res., 96, 6403–6414.

Crampin, S. & Zatsepin, S.V., 1997. Modelling the compliance of crustal rock—II. Response to temporal changes before earthquakes, Geophys. J. Int., 129, 495-506.

Crampin, S., Volti, T. & Stefansson, R., 1999. A successfully stress-forecast earthquake, Geophys. J. Int., 138, F1–F5.

Crampin, S. & Gao, Y., 2005. Comment on “Systematic analysis of shear-wave splitting in the aftershock zone of the 1999 Chi-Chi , Taiwan, earthquake: shallow crustal anisotropy and lack of precursory changes” by Yunfeng Liu, Ta-Liang Teng, and Yehuda Ben-Zion, Bull. Seism. Soc. Am., 95, 354-360.

Daley, T.M. & McEvilly, T.V., 1990. Shear wave anisotropy in the Parkfield Varian Well VSP, Bull. Seismol. Soc. Am., 80(4), 857–869.

Daneshvar, M. R., Clay, C. S. & Savage, M. K., 1995. Passive seismic imaging using microearthquakes, Geophysics, 60, 1178-1186.

Dieterich, J.H. & Kilgore, B.D., 1996. Imaging surface contacts: power law contact distributions and contact stresses in quarts, calcite, glass, and acrylic plastic, Tectonophysics, 256, 219–239.

Elkhoury, J. E., Brosky, E. E. & Agnew, D. C., 2006. Seismic waves increase permeability, Nature, 441, 1135-1138.

Field, E.H., Johnson, P.A., Beresnev, I.A. & Zeng, Y., 1997. Non-linear ground-motion amplification by sediments during the 1994 Northridge earthquake, Nature, 390, 599–602.

Gao, Y., Wang, P., Zheng, S., Wang, M. & Chen, Y.-T., 1998. Temporal changes in shear-wave splitting at an isolated swarm of small earthquakes in 1992 near Dongfang, Hainan Island, Southern China, Geophys. J. Int., 135, 102–112.

Hiramatsu, Y., Honma, H., Saiga, A., Furumoto, M. & Ooida, T., 2005. Seismological evidence on characteristic time of crack healing in the shallow crust, Geophys. Res. Lett., 32, L09304, doi:10.1029/2005GL022657.

Hung, J.-H., Wiltschko, D. V., Lin, H.-C., Hickman, J. B., Fang, P. & Bock, Y., 1999. Structure and motion of the southwestern Taiwan fold and thrust belt, TAO, 10 (3), 543-568.

Ikuta, R. & Yamaoka, K., 2004. Temporal variation in the shear wave anisotropy detected using the Accurately Controlled Routinely Operated Signal System (ACROSS), J. Geophys. Res., 109, B09305, doi:10.1029/2003JB002901.

Jin, A. & Aki, K., 1986. Temporal change in coda Q before the Tangshan earthquake of 1976 and the Haicheng earthquake of 1975, J. Geophys. Res., 91, 665–673.

Johnson, P.A. & Jia, X., 2005. Non-linear dynamics, granular media and dynamic earthquake triggering, Nature, 473, 871-874.

Johnson, P. A. & Sutin, A., 2005. Slow dynamics and anomalous fast dynamics in diverse solids, J. Acoust. Soc. Am., 117, 124-130.

Kanamori, H. & Fuis, G., 1976. Variation of P-wave velocity before and after the Galway Lake earthquake (ML=5.2) and the Goat Mountain earthquakes (ML=4.7, 4.7), 1975, in the Mojave desert, California, Bull. Seismol. Soc. Am., 66, 2027–2037.

Karabulut, H. & Bouchon, M., 2007. Spatial variability and non-linearity of strong ground motion near a fault, Geophys. J. Int., 170, 262-274, doi:10.1111/j.1365-246X.2007.03406.x.501.

Kuo, K. W., 1994. The geological character of the CWB Strong Motion Network: Chianan area, Central Weather Bureau Report, CW83-1A-12, 98 pp. (in Chinese).

Lee, C.-T., Cheng, C.-T., Liao, C.-W. & Tsai, Y.-B. 2001. Site classification of Taiwan free-field strong-motion stations, Bull. Seism. Soc. Am., 94 (5), 1283-1297.

Li, Y.-G., Vidale, J. E., Aki, K., Xu, F. & Burdette, T., 1998. Evidence of shallow fault zone strengthening after the 1992 M7.5 Landers, California, earthquake, Science, 279, 217-219.

Li, Y.-G., Chen, P., Cochran, E. S., Vidale, J. E. & Burdette, T., 2006. Seismic evidence for rock damage and healing on the San Andreas Fault associated with the 2004 M 6.0 Parkfield earthquake, Bull. Seism. Soc. Am., 96 (4B), S349-S363.

Liu, Y., Teng, T.-L. & Ben-Zion, Y., 2004. Systematic analysis of shear-wave splitting in the aftershock zone of the 1999 Chi-Chi , Taiwan, Earthquake: Shallow crustal anisotropy and lack of precursory variations, Bull. Seism. Soc. Am., 94, 2300-2347.

Liu, Y., Ben-Zion, Y. & Teng, T.-L., 2005a. Reply to "Comment on 'Systematic analysis of shear-wave splitting in the aftershock zone of the 1999 Chi-Chi, Taiwan, earthquake: shallow crustal anisotropy and lack of precursory changes,' by Yunfeng Liu, Ta-Liang Teng, and Yehuda Ben-Zion," by Stuart Crampin and Yuan Gao, Bull. Seism. Soc. Am., 95, 361-366.

Liu, Y., Teng, T.-L. & Ben-Zion, Y., 2005b. Near-surface seismic anisotropy, attenuation and dispersion in the aftershock region of the 1999 Chi-Chi Earthquake, Geophys. J. Int., 160, 695-706.

Liu, Y., Zhang, H., Thurber, C. & Roecker, S., 2008. Shear wave anisotropy in the crust around the San Andreas fault near Parkfield: spatial and temporal analysis, Geophys. J. Int., 172, 957-970.

Lyakhovsky, V., Ben-Zion, Y. & Agnon, A., 1997, Distributed damage, faulting and friction, J. Geophys. Res., 102, 27635–27649.

Lyakhovsky, V., Ben-zion, Y. & Agnon, A., 2005, A visco-elastic damage rheology and rate- and state-dependent friction, Geophys. J. Int., 161, 179–190, doi: 10.1111/j.1365-246X.2005.02583.x.

Ma, S., 2008. A physical model for widespread near-surface and fault zone damage induced by earthquakes, Geochemistry, Geophysics, Geosystems, 9, Q11009, doi:10.1029/2008GC002231.

Manga, M. & Brodsky, E., 2006. Seismic triggering of eruptions in the far field: Volcanoes and geysers, Annu. Rev. Earth Planet. Sci., 34, 263-291.

Manga, M. & Wang C.-Y., 2007. Earthquake hydrology, in Treatise on Geophysics, G. Schubert editor, volume 4, 293-320.

Marone, C., 1998. Laboratory-derived friction laws and their application to seismic faulting, Annu. Rev. Earth Planet. Sci., 26, 643-696.

Matsumoto, S., Obara, K., Yoshimoto, K., Saito, T., Ito, A. & Hasegawa, A., 2001. Temporal change in P-wave scatterer distribution associated with the M6.1 earthquake near Iwate volcano, northeastern Japan, Geophys. J. Int., 145, 48-58.

Mavko, G., Mukerji, T. & Dvorkin, J., 1998. The Rock Physics Handbook: Tools for Seismic Analysis of Porous Media, Cambridge University Press, 340 pp.

McEvilly, T.V. & Johnson, L.R., 1974. Stability of P and S velocities from central California quarry blasts, Bull. Seismol. Soc. Am., 64, 343–353.

Menke, W. & Schaff, D., 2004. Absolute earthquake locations with differential data, Bull. Seism. Soc. Am., 94, 2254-2264.

Munson, C.G., Thurber, C.H., Li, Y. & Okubo, P.G., 1995. Crustal shear wave anisotropy in southern Hawaii: Spatial and temporal analysis, J. geophys. Res., 100(B10), 20367–20377.

Niu, F., Silver, P.G., Nadeau, R.M. & McEvilly, T.V., 2003. Stress-induced migration of seismic scatterers associated with the 1993 Parkfield aseismic transient event, Nature, 426, 544–548.

Niu, F., Silver, P.G., Daley, T., Cheng, X. & Majer, E., 2008. Preruptur dilatancy observed from active source monitoring at the Parkfield SAFOD drill site, Nature, 454, doi:10.1038/nature07111.

Nur, A. & Simmons, G., 1969. The effect of saturation on velocity in low porosity rocks, Earth Planetary Sci. Lett., 7, 183-193.

Nuttli, O., 1961. The effect of the Earth's surface on the S wave particle motion, Bull. Seism. Soc. Am., 51, 2, 237-246.

Peng, Z. & Ben-Zion, Y., 2004. Systematic analysis of crustal anisotropy along the Karadere-Duzce branch of the North Anatolian fault, Geophys. J. Int., 159, 253-274.

Peng, Z. & Ben-Zion, Y., 2005. Spatio-temporal variations of crustal anisotropy from similar events in aftershocks of the 1999 M7.4 İzmit and M7.1 Duzce, Turkey, earthquake sequences, Geophys. J. Int., 160, 1027-1043.

Peng, Z. & Ben-Zion, Y., 2006. Temporal changes of shallow seismic velocity around the Karadere-Duzce branch of the north Anatolian fault and strong ground motion, Pure Appl. Geophys., 163, 567-599, doi: 10.1007/s00024-005-0034-6.

Poupinet, G., Ellsworth, W.L., & Frechet, J., 1984. Monitoring velocity variations in the crust using earthquake doublets: An application to the Calaveras Fault, California, J. Geophys. Res., 89, 5719–5731.

Press, W., Flannery, B., Teukolsky, S. & Vetterling, W., 1986. Numerical Recipes, Cambridge University Press, Cambridge.

Rojstaczer, S.A., Wolf, S.C. & Michel, R.L., 1995. Permeability enhancement in the shallow crust as a cause of earthquake-induced hydrological changes, Nature, 373, 237–239.

Rubinstein, J.L. & Beroza, G.C., 2004a. Evidence for Widespread Nonlinear Strong Ground Motion in the Mw 6.9 Loma Prieta Earthquake, Bull. Seism. Soc. Am., 94, 1595-1608.

Rubinstein, J.L. & Beroza, G.C., 2004b. Nonlinear strong ground motion in the ML5.4 Chittenden earthquake: Evidence that pre-existing damage increases susceptibility to further damage, Geophysics. Res. Lett., 31, L23614, doi:10.1029/2004GL021357.

Rubinstein, J.L. & Beroza, G.C., 2005. Depth constraints on nonlinear strong ground motion, Geophysics. Res. Lett., 32, L14313, doi:10.1029/2005GL023189.

Rubinstein, J.L., Uchida, N. & Beroza, G.C., 2007. Seismic velocity reductions caused by the 2003 Tokachi-Oki earthquake, J. Geophys. Res., 112, B05315, doi: 10.1029/2006JB004440.

Saiga, A., Hiramatsu, Y., Ooida, T. & Yamaoka, K., 2003. Spatial variation in the crustal anisotropy and its temporal variation associated with a moderate-sized earthquake in the Tokai region, central Japan, Geophys. J. Int., 154, 695–705.

Savage, M. K., Peppin, W. A. & Vetter, U. R., 1990. Shear wave anisotropy and stress direction in and near Long Valley Caldera, California, 1979-1988, J. Geophys. Res., 95(B7), 11165-11177.

Sawazaki, K., Sato, H., Nakahara, H. & Nishimura, T., 2006. Temporal change in site response caused by earthquake strong motion as revealed from coda spectral ratio measurement, Geophys. Res. Lett., 33, L21303, doi: 10.1029/2006GL027938.

Sawazaki, K., Sato, H., Nakahara, H. & Nishimura, T., 2008. Drop and recovery process of seismic velocity in the shallow ground caused by strong ground motion shock as revealed from coda deconvolution analysis, Bull. Seism. Soc. Am., in press.

Schaff, D. P. & Beroza, G. C., 2004. Coseismic and postseismic velocity changes measured by repeating earthquakes, J. Geophys. Res., 109, B10302, doi:10.1029/2004JB003011.

Scholz, C.H., 1968. The frequency-magnitude relation of microfracturing in rock and its relation to earthquakes, Bull. Seism. Soc. Am., 58, 399-415.

Scholz, C.H., 2002. The Mechanics of Earthquakes and Faulting, 2nd edn, Cambridge University Press, New York, 471 pp.

Silver, P.G., Daley, T.M., Niu, F. & Majer, E.L., 2007. Active source monitoring of cross-well seismic travel time for stress-induced changes, Bull. Seism. Soc. Am., 97, 1B, 281–293, doi: 10.1785/0120060120.

Tadokoro, K. & Ando, M., 2002. Evidence for rapid fault healing derived from temporal changes in S wave splitting, Geophys. Res. Lett., 29(4), 1047, doi: 10.1029/2001GL013644.

Taira, T., Silver, P.G., Niu, F. & Nadeau, R.M., 2008a. Detecting seismogenic stress evolution and constraining fault zone rheology in the San Andreas Fault following the 2004 Parkfield earthquake, J. Geophys. Res., 113, B03303, doi: 10.1029/2007JB005151.

Taira, T., Silver, P.G., Niu, F. & Nadeau, R.M., 2008b. Seismic evidence for remote triggering of fault-strength changes on the San Andreas fault at Parkfield, Nature, in revision.

Tai-Tech, Geotechnical & Construction Co., Ltd., 2000. The hydrogeological survey and liquefaction analysis report, National Taiwan University, Taipei (In Chinese).

TenCate, J. A., Smith, E. & Guyer, R. A., 2000. Universal slow dynamics in granular solids, Phys. Rev. Lett., 85, 1020–1023.

Toteva, T., Peng, Z. & Zhao, P., 2008. Temporal changes in near-surface layers and deep fault zone scatterers after the 2004 Mw6.0 Parkfield earthquake observed by the UPSAR, Eos Trans. AGU, 89(53), Fall Meet. Suppl., Abstract S53A-1816.

Wang, C.-Y., Wang, C.-H. & Manga, M, 2004. Coseismic release of water from mountains: Evidence from the 1999 (Mw = 7.5) Chi-Chi, Taiwan, earthquake, Geology, 32(9), 769-772.

Wang, C.-Y. & Chia, Y. 2008. Wenchuan earthquake enhanced crustal permeability in Taiwan, Eos Trans. AGU, 89(53), Fall Meet. Suppl., Abstract U23B-0065.

Wen, S., Chen, C.-H. & Teng, T.-L., 2007. Ruptures in a highly fractured upper crust, Pure Appl. Geophys., 165, 201-213, doi: 10.1007/s00024-008-0297-9.

Wessel, P. & Smith, W.H.F., 1998. New, improved version of the Generic Mapping Tools released, EOS, Trans. Am. Geophys. Un., 79, 579.

Whitcomb, J.H., Garmany, J.E. & Anderson, D.L., 1973. Earthquake prediction: variation of seismic velocities before the San Francisco earthquake, Science, 180, 632–635.

Wu, Y.-M. & Teng, T.-L., 2002. A virtual subnetwork approach to earthquake early warning, Bull. Seism. Soc. Am., 92, 2008-2018.

Wu, C., Peng, Z. & Ben-Zion, Y., 2008a. Non-linearity and temporal changes of fault zone site response associated with strong ground motion, Geophys. J. Int., doi: 10.1111/j.1365-246X.2008.04005.x, in press.

Wu, C., Peng, Z. & Assimaki, D., 2008b. Systematic analysis of temporal changes in site response associated with strong ground motion in Japan, Eos Trans. AGU, 89(53), Fall Meet. Suppl., Abstract S51E-08.

Yu, S.-B., Kuo, L.-C., Hsu, Y.-J., Su, H.-H., Liu, C.-C., Hou, C.-S., Lee, J.-F., Lai, T.-C., Liu, C.-C., Liu, C.-L., Tseng, T.-F., Tsai, C.-S. & Shin, T.-C., 2001. Preseismic deformation and coseismic displacements associated with the 1999 Chi-Chi, Taiwan, earthquake, Bull. Seism. Soc. Am., 91, 995-1012.

Zhao, P. & Peng, Z., 2008. Identification of repeating earthquakes and spatio-temporal variations of fault zone properties around the Parkfield section of the San Andreas fault and the central Calaveras fault, Eos Trans. AGU, 89(53), Fall Meet. Suppl., Abstract S53A-1817.